

See discussions, stats, and author profiles for this publication at: <https://www.researchgate.net/publication/262338574>

# Synthesis, crystal structure and antiproliferative activity of Cu(II) nalidixic acid–DACH conjugate: Comparative in vitro DNA/RNA binding profile, cleavage activity and molecular d...

ARTICLE *in* EUROPEAN JOURNAL OF MEDICINAL CHEMISTRY · MAY 2014

Impact Factor: 3.45 · DOI: 10.1016/j.ejmech.2014.04.080 · Source: PubMed

---

CITATIONS

5

---

READS

102

4 AUTHORS, INCLUDING:



Farukh Arjmand

Aligarh Muslim University

111 PUBLICATIONS 1,359 CITATIONS

SEE PROFILE



Taibi Ben Hadda

Université Mohammed Premier

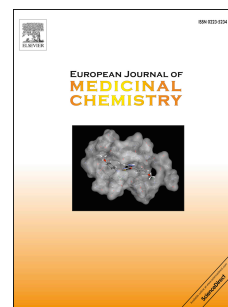
338 PUBLICATIONS 1,437 CITATIONS

SEE PROFILE

# Accepted Manuscript

Synthesis, crystal structure and antiproliferative activity of Cu(II) nalidixic acid–DACH conjugate: Comparative *in vitro* DNA/RNA binding profile, cleavage activity and molecular docking studies

Farukh Arjmand, Imtiaz Yousuf, Taibi ben Hadda, Loic Toupet



PII: S0223-5234(14)00409-7

DOI: [10.1016/j.ejmech.2014.04.080](https://doi.org/10.1016/j.ejmech.2014.04.080)

Reference: EJMECH 6951

To appear in: *European Journal of Medicinal Chemistry*

Received Date: 15 February 2014

Revised Date: 27 April 2014

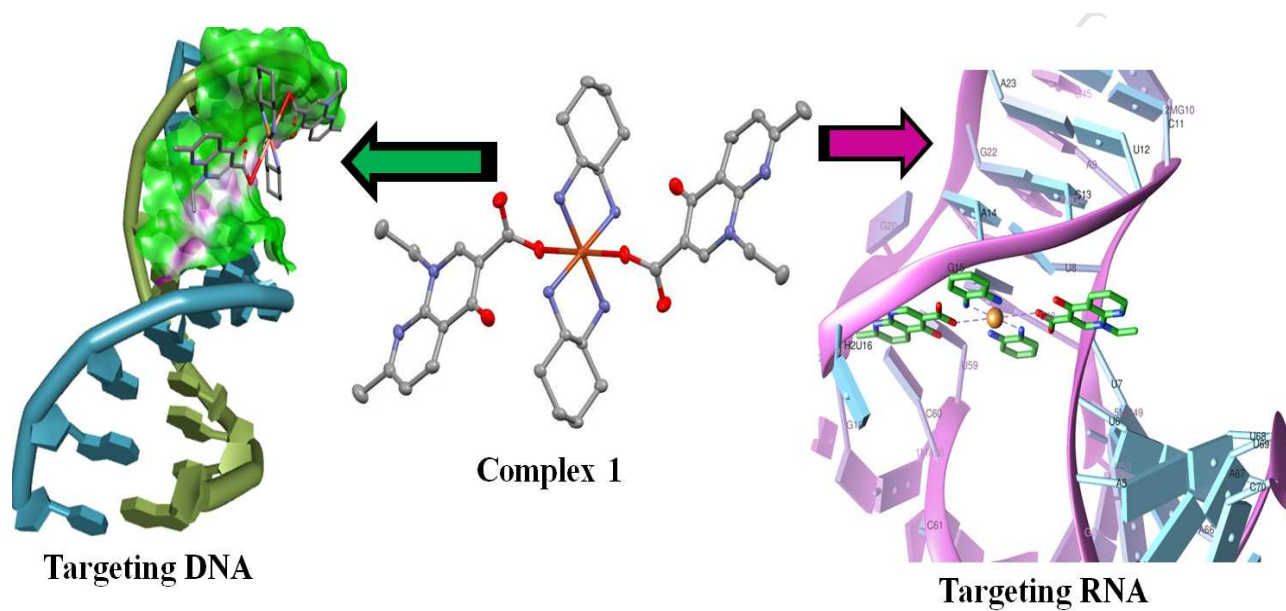
Accepted Date: 29 April 2014

Please cite this article as: F. Arjmand, I. Yousuf, T.b. Hadda, L. Toupet, Synthesis, crystal structure and antiproliferative activity of Cu(II) nalidixic acid–DACH conjugate: Comparative *in vitro* DNA/RNA binding profile, cleavage activity and molecular docking studies, *European Journal of Medicinal Chemistry* (2014), doi: 10.1016/j.ejmech.2014.04.080.

This is a PDF file of an unedited manuscript that has been accepted for publication. As a service to our customers we are providing this early version of the manuscript. The manuscript will undergo copyediting, typesetting, and review of the resulting proof before it is published in its final form. Please note that during the production process errors may be discovered which could affect the content, and all legal disclaimers that apply to the journal pertain.

## Graphical Abstract

Targeting DNA and RNA by molecular docking studies.



# Synthesis, crystal structure and antiproliferative activity of Cu(II) nalidixic acid–DACH conjugate: Comparative *in vitro* DNA/RNA binding profile, cleavage activity and molecular docking studies

Farukh Arjmand <sup>a,\*</sup>, Imtiyaz Yousuf <sup>a</sup>, Taibi ben Hadda <sup>b</sup>, Loic Toupet <sup>c</sup>

<sup>a</sup>Department of Chemistry, Aligarh Muslim University, Aligarh 202002, Uttar Pradesh, India.

<sup>b</sup>Laboratoire Chimie des Matériaux, FSO, Université Mohammed I, Oujda 60000, Morocco.

<sup>c</sup>Institut de Physique de Rennes, UMR 625, Université de Rennes 1, Campus de Beaulieu Bat. 11 A, 263 av. Général Leclerc, 35042 Rennes Cedex, France.

\*Corresponding author. Tel.: +91 5712703893.

E-mail address: farukh\_arjmand@yahoo.co.in (F. Arjmand)

## Abstract

Nalidixic acid–DACH conjugate Cu(II) molecular entity, **1** was synthesized, thoroughly characterized by spectroscopic techniques (FT–IR, EPR and ESI–MS) and single crystal X–ray diffraction technique as a potential chemotherapeutic drug candidate for cancer oncology. Complex **1** was found to be a potent drug–like molecular entity in confirmation with Lipinski rules. 1*R*,2*R*–diaminocyclohexane (DACH) ligand scaffold (which reduces the drawbacks of cisplatin analogues) and nalidixic acid pharmacophore make it a suitable drug entity targeting nucleic acids. To evaluate the chemotherapeutic potential of **1** comparative *in vitro* DNA/RNA interaction studies have been investigated by employing various biophysical techniques (UV–vis, fluorescence, circular dichroism, viscosity, cyclic voltammetry and FT–IR), cleavage activity and Topo–II inhibition assay. Further, mechanistic investigation revealed the efficiency of **1** to cleave pBR322 DNA strands by an oxidative pathway involving the generation of ROS and preferential selectivity towards the A–T region of DNA major groove. Antiproliferative activity in conjugation with flow cytometry analysis of **1** against human osteoblastoma cell line (U2OS)

suggested a cell cycle arrest at S phase. This work further advances our knowledge for the development and design of small RNA targeted therapeutic molecules which are under exploited drug targets.

**Keywords:** Nalidixic acid; pBR322 DNA cleavage; Topo-II inhibition assay; U2OS cells; Molecular docking studies

### Abbreviations

UV-vis	UV-visible
ct-DNA	Calf thymus DNA
Topo II	Topoisomerase II
U2OS	Human osteoblastoma cell line

### 1. Introduction

There has been tremendous drive for the development of efficient, less toxic and selective metal-based drugs in chemotherapy, which could overcome the disadvantages of cisplatin, namely systemic toxicity-related issues and drug resistance [1–3]. Traditionally, many metal-based anticancer drugs have been designed to target DNA for chemotherapeutic purposes [4,5]. Owing to the fact, that DNA is not always primary target for certain metal based anticancer compounds as they can also bind more strongly to proteins or enzymes than to DNA [6], therefore there is much focus on efficient targeting strategies to deliver metallodrugs selectively at the site of action. Ribonucleic acid (RNA) offers several advantages as attractive target for therapeutic intervention in drug discovery in comparison to DNA due to its unique three dimensional (3D) pockets for specific binding for small ligands [7,8]. Moreover, it is involved in many cellular processes, from regulation of gene expression to protein synthesis [9]. There are well documented classes of compounds that can modulate RNA function which includes antibiotics [10] (such as tetracycline, heterocyclic quinolone), small synthetic peptide motifs [11]

and metal-based compounds [12–14] targeting RNA with good affinity and specificity. More recently miRNAs have emerged as therapeutic targets for cancer therapy since the abnormal expression of these noncoding RNAs is associated with the pathogenesis of human cancer [15,16].

Nalidixic acid—first generation drug of quinolone family, has been extensively explored for broad spectrum of biological activities like antimicrobial [17], anti-inflammatory [18], antiproliferative [19] and antitumor [20–22] etc. During the past, many metal based nalidixic acid complexes were synthesized [23–25] either as binary or ternary complexes with one or more O ( $\text{H}_2\text{O}$ , MeOH) or N donor ligands or co-ligands (pyridine, 2,2' bipyridine, DACH, etc.) due to the synergistic activity of metal ion to quinolone drugs with improved pharmacological activity [26]. 1*R*,2*R*-diaminocyclohexane (DACH) significantly improves the pharmacological efficacy of Pt drugs (oxaliplatin) by increasing cellular uptake and inhibiting DNA mismatch repair [27], therefore it is a suitable carrier ligand which has been effectively utilized in modulation of new therapeutic chemical entities.

Copper(II) complexes with DNA and RNA recognition properties represent important chemotypes capable of abrogating nucleic acid sequences through metal-driven oxidative cleavage [28]. Copper toxicity comes from its ability to produce reactive oxygen species (ROS), to displace other metal ions, to peroxide lipids or directly to cleave DNA and RNA [29]. The rationale for using copper complexes as anti-cancer agents is to avoid severe side effects induced by known anticancer agents like cisplatin as the endogenous metals like Cu(II) are considered to be less toxic for normal cells with respect to cancer cells. More recently, several synthetic Cu(II) complexes have been studied as pharmacological and potential anticancer agents

[28] which further demonstrated that these copper complexes can trigger cancer cell death through apoptotic and non apoptotic (paraptosis) mechanisms [30–33].

In continuity to our research efforts for developing new efficacious metal-based chemotherapeutic agents for cancer oncology [34], we report herein the synthesis, characterization and single X-ray diffraction of Cu(II) nalidixic acid-DACH conjugate (**1**). We have carried out the comparative *in vitro* interaction studies with RNA and DNA targets. Interestingly, we found that the complex **1** exhibited more avid binding propensity towards RNA, thereby was better suited for RNA targeting as compared to DNA. Additionally, Topo II inhibition assay was carried out as the main target of quinolone drugs is gyrase type II topoisomerase enzyme that participates in DNA replication. Topo II-targeting agents have been shown to produce enzyme linked DNA breaks by trapping the covalent reaction intermediate (cleavable complex). This ‘cleavable complex’ is presumed to be initial event that triggers cellular responses leading to cell death (Topo poisons) [35]. However, ‘cleavable complex’ formation may not be the sole mechanism of cell killing by Topo II targeting drugs as they may also show catalytic inhibitory activity by binding to the ATPase domain of Topo II (Topo inhibitors) [36]. Furthermore, the antiproliferative activity in conjugation with flow cytometry analysis of complex **1** against human bone marrow cell line was also studied. It was observed that complex **1** inhibited the proliferation of cultured U2OS cells with a dramatic increase of S phase cells indicative of a delay or inhibition of cell cycle progression through S phase arrest.

Complex **1** exhibits novelty as a potential antitumor chemotherapeutic agent owing to the following properties i) fairly good water-solubility ii) better cellular uptake due to high lipophilicity iii) quinolone drug pharmacophore iv) hydrogen bond acceptors <10, hydrogen donors site <5 and v) clogP <5. The calculated molecular pharmacokinetic properties of complex

**1** by Osiris and Molinspiration servers [37] revealed moderate tendency towards drug-likeness and drug score with no toxicity (Fig. S1a and b).

## 2. Results and discussion

### 2.1. Synthesis and characterization

Complex **1** was synthesized by reacting methanolic solutions of nalidixic acid (deprotonated with KOH), 1*R*, 2*R*-diaminocyclohexane and CuCl<sub>2</sub> · 2H<sub>2</sub>O in 2:2:1 stoichiometric ratio as depicted in Scheme 1. The synthesized complex was air-stable and was found soluble in H<sub>2</sub>O and organic solvents like, DMF and DMSO. The molar conductance value of **1** ( $1 \times 10^{-3}$  M) in DMSO suggested its non-electrolytic nature. The structure of **1** has also been authenticated by single crystal X-ray diffraction technique. Further, **1** was also characterized by FT-IR, UV-vis, EPR, ESI-MS and elemental analysis, that corroborate well with the structure proposed by single-crystal X-ray diffraction technique.

### 2.2. Description of the X-ray crystal structure

Single crystal X-ray determination at 140 K revealed that complex **1** was successfully solved and converged in the triclinic space group *P*-1. The complex is a mononuclear with central Cu(II) ion coordinated to two  $\text{naI}^-$  units (*via* carboxylate oxygen) and two chelating neutral DACH groups. The Cu(II) ion is located on a symmetry center and has the overall geometry of a slightly tetragonally distorted octahedron. An equatorial plane is formed by four N atoms of two DACH ligand moieties while the axial Jahn-Teller positions are occupied by two carboxylate O atoms of two  $\text{naI}^-$  ligand units that are arranged in a trans fashion (Fig. 1a). Thus a coordination environment of  $\text{CuN}_4\text{O}_2$  unit is formed having Cu1–O1 = 2.471 Å, Cu1–N1 = 2.009(19) and Cu1–N2 = 2.001(18) Å. Atoms N1 and N2 are bonded to Cu(II) *via* a five membered chelate ring (C1/N1/Cu1/N2/C2) while DACH adopts a half-chair conformation. The selected bond lengths



and bond angles are listed in Table S1. All the Cu–O and Cu–N bond distances have been found within the range reported for octahedral Cu(II) complexes. The NH<sub>2</sub> groups of the DACH ligands participate in inter/intra-molecular hydrogen bonding interactions with carboxylato and pyridone O atoms of naI<sup>−</sup> moiety having O1·····N1 = 3.022 Å°, O1·····N2 = 2.051 Å° (inter-molecular) and O2·····N1 = 2.974 Å°, O3·····N2 = 2.992 Å° (intra-molecular) hydrogen bonding (Fig. 1b). The coordination geometry is distorted from regular octahedral as a consequence of the small bite angle of DACH ligand with N(1)#1–Cu(1)–N(2)#1=84.51(7).

### 2.3. IR spectroscopy

IR spectroscopy provides an insight about the structural, characterization and the coordination modes of metal complexes. The IR spectrum of nalidixic acid (HnaI) displayed absorption bands at 3385, 1628 and 1386 cm<sup>−1</sup> attributable to the  $\nu(\text{O-H})$ ,  $\nu_{\text{asym}}(\text{C=O})_{\text{carboxylic}}$  and  $\nu_{\text{sym}}(\text{C=O})_{\text{carboxylic}}$  stretching vibrations, respectively. However, in the IR spectrum of complex **1** the absence of a peak at 3385 cm<sup>−1</sup> confirmed its deprotonation and coordination to metal ion, while the characteristic peaks corresponding to  $\nu_{\text{asym}}(\text{C=O})$  and  $\nu_{\text{sym}}(\text{C=O})$  stretching vibrations of the carboxylato group were shifted to 1632 cm<sup>−1</sup> and 1425 cm<sup>−1</sup>, respectively. The calculated value,  $\Delta\nu = [\nu_{\text{asym}}(\text{C=O}) - \nu_{\text{sym}}(\text{C=O})]$ , a useful characteristic aid for predicting the coordination mode of carboxylato ligand suggested a value 207 cm<sup>−1</sup> for **1** that implicated monodentate coordination mode for the nalidixic acid moiety [38]. A diagnostic absorption peak associated with the  $\nu(\text{NH}_2)$  stretching vibrations of DACH ligand was found at ca. 3127 cm<sup>−1</sup>. Additional absorption frequency bands at 2922 cm<sup>−1</sup> corresponded to  $\nu(\text{CH}_2)$  vibrations of the cyclohexyl ring. The formation of complex **1** was further ascertained by the presence of medium intensity bands at 537 and 429 cm<sup>−1</sup> corresponding to Cu–N and Cu–O vibrations, respectively.

### 2.4. EPR spectroscopy

X-Band EPR measurements of complex **1** was recorded in DMSO at liquid nitrogen temperature at frequency 9.1 GHz under the magnetic field strength of 3000 G. The  $g$  values were calculated from the spectra given in Fig. S2 using the formula  $g_{av}^2 = g_{\parallel}^2 + 2g_{\perp}^2/3$ , depicted  $g_{\parallel} = 2.172$ ,  $g_{\perp} = 2.065$  and  $g_{av} = 2.10$ , thereby suggesting an octahedral geometry. The trend  $g_{\parallel} > g_{\perp} > g_e$  (2.0023) revealed that the unpaired electron should be located in the  $d_{x^2-y^2}$  orbital of the Cu(II) ion characteristic of axial symmetry [39]. Further,  $g_{\parallel}$ , a parameter sensitive enough to indicate covalence predicted an appreciable metal–ligand covalent character with  $g_{\parallel} < 2.3$  for complex **1**.

### 2.5. Electronic spectra

The electronic spectrum of the complex in aqueous solution exhibited well resolved bands at 263 and 328 nm region assignable to  $\pi-\pi^*$  and  $n\rightarrow\pi^*$  ligand centered transitions. The appearance of a broad d–d transition envelope at  $\lambda_{max}$  630 nm in the visible spectrum was consistent with the tetragonally distorted octahedral environment around Cu(II) center [40].

### 3. Comparative *in vitro* DNA/RNA binding studies

Small molecules that show therapeutic potential are most likely to be targeted to DNA rather than RNA and most of the previous studies were pertaining to metal complex–DNA interactions. Unlike DNA, RNA can fold into diverse structures that offers potential binding pockets similar to proteins; form well–defined structures like double helices, hairpins, bulges, and pseudoknots, which offer structural bases for new therapeutic agents, thus its unique structural diversity could be exploited to design drug entities that specifically target RNA. Essentially, the mechanism of binding for DNA and RNA by cationic complexes is different, as DNA is targeted by drugs often by direct incorporation in the double helix or *via* covalent modification or cleavage of DNA; however RNA binding involves typically by non–covalent interactions such as electrostatic, hydrogen bonding, van der Waals interaction and with no direct coordination. Moreover, metal

complexes that are coordinatively saturated, inert to substitution, having rigid and well defined structure are better suited for RNA targeting [8]. In lieu of this principle, comparative study of drug candidates towards ct-DNA and tRNA could be instrumental for drug design especially in the area of cancer therapeutics.

### 3.1. UV-vis absorption titrations

Electronic absorption spectroscopy is one of the most widely used techniques to study the metal complex–nucleic acid interactions. The electronic absorption spectral changes of complex **1** in absence and presence of ct-DNA or yeast tRNA are illustrated in Fig. 2a and b, at 263 nm ascribed to intraligand transitions. Addition of increasing concentrations of nucleic acids ( $0.00$ – $5.00 \times 10^{-5}$  M) to a fixed concentration of complex ( $1.0 \times 10^{-5}$  M) exhibited an evident “hyperchromaticity” of 33 % and 39 % for ct-DNA and yeast tRNA, respectively along with a slight red shift of 2 nm. The observed “hyperchromic” spectral changes, suggested that the complex **1** exhibited good binding propensity for ct-DNA and yeast tRNA, although the extent of hyperchromism was greater with tRNA, therefore greater binding affinity; binding mode could be electrostatic *via* external contact or groove binding which can also be substantiated from the probability of hydrophobic interactions involving the alkyl groups of  $\text{Na}^+$  moieties with the nucleic acid surfaces. Additionally, the binding interactions can be stabilized by hydrogen–bonding interactions between  $-\text{NH}_2$  group or pyridone oxygen atoms of complex **1** with the nucleobases, that are accessible both in the major and minor grooves.

In order to compare quantitatively the binding strength of complex **1** with ct-DNA and yeast tRNA, intrinsic binding constant  $K_b$  values of the complex were determined by monitoring changes in absorbance with increasing concentration of ct-DNA and yeast tRNA given by Eq.1

$$\frac{[\text{DNA or RNA}]}{(\varepsilon_a - \varepsilon_f)} = \frac{[\text{DNA or RNA}]}{(\varepsilon_b - \varepsilon_f)} + \frac{1}{K_b(\varepsilon_b - \varepsilon_f)} \quad (1)$$

where [DNA or RNA] are the DNA or RNA concentration, and  $\varepsilon_a$ ,  $\varepsilon_f$  and  $\varepsilon_b$  are the apparent ( $A_{\text{abs}}/[\text{complex } \mathbf{1}]$ ), free and bound complex extinction coefficients, respectively. In a plot of [DNA or RNA]/( $\varepsilon_a - \varepsilon_f$ ) vs. [DNA or RNA] with a slope of  $1/(\varepsilon_b - \varepsilon_f)$  and intercept of  $1/[K_b(\varepsilon_b - \varepsilon_f)]$ ,  $K_b$  values were obtained by the ratio of the slope to the intercept. The intrinsic binding constant  $K_b$  values for complex **1** with ct-DNA or yeast tRNA were calculated and found to be  $5.12(\pm 0.15) \times 10^4$  and  $8.16(\pm 0.09) \times 10^4 \text{ M}^{-1}$ , respectively.

The  $K_b$  values demonstrated stronger binding propensity of **1** with yeast tRNA as compared to ct-DNA owing to reasons i) yeast tRNA which exhibits A-form conformations with L-shaped tertiary structure has a wide shallow minor groove and pulled-in narrow major groove allowing its base pairs to remain well exposed and easily accessible for the drug entities and ii) complex **1** could bind in the bulge region of yeast tRNA, thereby providing a rationale for its stronger binding affinity [41].

### 3.2. Emission spectral titration

In the absence of ct-DNA or yeast tRNA, complex **1** displayed a luminescence in Tris-HCl buffer with a fluorescence maxima appearing at 370 nm upon excitation by 270 nm light. Upon progressive addition of ct-DNA or yeast tRNA ( $0.00\text{--}3.69 \times 10^{-5} \text{ M}$ ) to a fixed concentration of complex **1** ( $1.67 \times 10^{-5} \text{ M}$ ), resulted an enhanced fluorescence emission intensity with no apparent change in the shape and position of the emission bands (Fig. 3a and b). The observed enhancement in emission spectra upon binding of the complex **1** with ct-DNA or yeast tRNA is largely due to the change in the environment of the metal complex from polar to non-polar and is related to the extent to which a complex penetrates into the hydrophobic environment of the

nucleic acids. Moreover, nucleic acids being hydrophobic macromolecules are capable of preventing the quenching effects that result from the energy changes occurring during the course of collisions between the metal complex and solvent molecules [42]. The binding constant,  $K$  as quantified by Scatchard equation [43] were found out to be  $4.63 \times 10^4$  and  $7.46 \times 10^4 \text{ M}^{-1}$  for ct-DNA and yeast tRNA, respectively with a mean standard deviation of  $\pm 0.13$ .

### 3.3. EB competition assay

To get a further insight about the interaction mode of complex **1** with ct-DNA and yeast tRNA, steady state competitive binding experiments using EB as a fluorescent probe were carried out. EB emits fluorescence in presence of DNA or RNA due to its strong interaction between adjacent base pairs. The enhanced fluorescence intensity of EB gets evidently quenched when a second molecule displaces the bound EB molecule from EB-DNA or EB-RNA complex by decreasing the number of binding sites. Thus, the ability of a complex to affect the fluorescence intensity of EB in EB-DNA or EB-RNA adduct can be used as a reliable tool to measure its extent of binding with DNA/RNA. Upon progressive addition of complex **1** to ct-DNA or yeast tRNA, pretreated with EB such that the ratio, [complex **1**]/[DNA or RNA] changed from 1:1 to 8:1, a decrease in emission intensity was observed indicative of competition between EB and complex **1** towards ct-DNA or yeast tRNA binding (Fig. S3a and b). However, this decrease in intensity is much lesser as compared to classical intercalators [44] thus ruling out the possibility of an intercalative mode and predicting a groove binding nature of complex **1**. To quantitatively assess the magnitude of interaction, classical Stern–Volmer equation was employed:

$$I_0/I = 1 + K_{sv}.r \quad (2)$$

where  $I_0$  and  $I$  represent the fluorescence intensities in the absence and presence of complex **1** respectively;  $r$  is the concentration ratio of complex **1** to DNA or RNA.  $K_{sv}$  is used to evaluate

the quenching efficiency and is obtained as the slope of  $I_0/I$  vs.  $r$ , Stern–Volmer constant,  $K_{sv}$  were calculated and found to be 1.32 and 2.38 for ct–DNA and yeast tRNA respectively, indicating the stronger affinity of **1** with tRNA as compared to ct–DNA.

### 3.4. Circular dichorism

Circular dichorism (CD) is a sensitive technique used to elucidate the changes in the secondary structure of inherently chiral biomolecules like nucleic acids upon interaction with small molecules (often organic ligands or metal complexes). In case of ct–DNA, the bands in the CD spectrum emanate from the base stacking interactions and the double helical suprastructure of the polynucleotide, thereby provide asymmetric environments for the nucleobases [45]. CD spectrum of B–DNA exhibits a positive band at 270 nm (base stacking) and a negative band at 245 nm (helicity). Simple groove binding and electrostatic interaction of the complexes can lead to slight perturbation of the intrinsic CD profile of DNA; On the other hand an intercalating molecule enhances the intensities of both bands due to disruption of the stacking of the nucleobases on intercalation [46]. Upon addition of complex **1** to ct–DNA, ( $r = [\text{complex } \mathbf{1}]/[\text{DNA}] = 1$ ), the CD spectrum undergoes decrease in intensity in both the positive and negative bands, suggesting that the complex **1** can unwind the DNA helix that lead to loss of the helicity (Fig. S4a).

The CD spectrum of tRNA depicts the characteristic four major peaks at 210 and 243 nm (negative), 227 and 270 nm (positive) which is consistent with A–conformation of tRNA [47,48]. Upon addition of complex **1** to tRNA solution ( $r = [\text{complex } \mathbf{1}]/[\text{tRNA}] = 1$ ) a significant increase in the amplitude of a negative band at 210 nm was observed while positive bands at 227 and 270 nm showed relatively less decrease in intensities with less or no band shifting (Fig. S4b). The reduced intensity of the band at 270 nm, in the spectra of complex **1**–tRNA system together

with the major intensity changes of the bands at 210 and 227 nm could be due to the tRNA aggregation and its particle formation [49].

### 3.5. Viscosity measurements

Viscosity experiment is an effective tool to detect binding modes between small molecules and DNA and is usually done to clarify the mode of binding. Well-known DNA intercalators like EB, causes DNA helix to increase its length by separating its base pairs to accommodate itself, resulting an increase in viscosity. However, complexes that bind either electrostatically *via* sugar-phosphate backbone produce bends or kinks in the DNA helix reducing its effective length and its viscosity, while DNA groove binding under the identical experimental conditions essentially results in little or no effect on DNA viscosity. Plots of relative viscosity  $(\eta/\eta_o)^{1/3}$  vs. [Compound]/[DNA] shown in Fig. S5 exhibited only a minor change in relative specific viscosity indicating groove or partial intercalative binding of complex **1** towards ct-DNA. However, in case of EB, the viscosity increased notably upon increasing its concentration suggestive of intercalation as a binding mode [50]. In contrast, no obvious change in relative viscosity was observed for yeast tRNA upon addition of complex **1** owing to its non-linear L-shaped tertiary structure [51].

### 3.6. Cyclic voltammetry

In order to provide the complement to the previously used spectroscopic methods of **1**-DNA/RNA interaction, *in vitro* redox behavior of complex **1** in the absence and presence of nucleic acids (DNA/RNA) was studied by using cyclic voltammetry. The cyclic voltammogram of complex **1**, in the absence of DNA/RNA and at a scan range of 0.2 Vs<sup>-1</sup> exhibited a quasireversible redox wave for a one-electron transfer process corresponding to the Cu(II)/Cu(I) redox couple with an anodic peak potential,  $E_{pa}$  of -0.12 V and a cathodic peak potential,  $E_{pc}$  of

–0.68 V. The difference between cathodic and anodic peak potential,  $\Delta E_p$  and ratio of anodic and cathodic peak currents,  $I_{pa}/I_{pc}$  were found to be –0.56 V and 0.91, respectively. The formal potential,  $E_{1/2}$  taken as an average of  $E_{pa}$  and  $E_{pc}$  values was calculated to be –0.40 V in the absence of DNA/RNA. However, upon addition of ct–DNA and yeast tRNA to **1** under same experimental conditions resulted in significant perturbations in cathodic and anodic peak current due to slow diffusion of an equilibrium mixture of the free and DNA/RNA bound complex to the electrode surface, (Fig. S6a and b) [52]. The  $I_{pa}/I_{pc}$  values were shifted to 0.80 and 0.75 for ct–DNA and yeast tRNA respectively, while  $E_{1/2}$  values shifted to less negative potentials for both RNA (–0.33 V) and DNA (–0.36 V). The negative shift in the peak potential values observed in the presence of nucleic acids,  $\Delta E_p$  (–0.50 V for DNA and –0.44 V for RNA) demonstrated electrostatic type of interactions involving groove binding of complex **1** with the nucleic acids [53]. Moreover, the larger shifts in  $\Delta E_p$ ,  $E_{1/2}$ , and  $I_{pa}/I_{pc}$  values observed for **1**–yeast tRNA complex than **1**–ct–DNA revealed greater binding propensity of **1** towards yeast tRNA.

### 3.7. Interaction studies by FT–IR spectroscopy

IR spectroscopy was used to study the Complex **1**–DNA/RNA interactions in the mid IR frequency bands. Significant spectral changes in the shape and position of vibration band(s) corresponding to the different nitrogenous bases of ct–DNA in the presence of complex **1** were observed. As depicted in Fig. S7a, shift of the guanine band at  $1710\text{ cm}^{-1}$  (guanine–C=O stretch) to a lower frequency at  $1690\text{ cm}^{-1}$  for **1**–DNA complex was observed. Another important shift and intensity variations was observed in the thymine band (thymine–O2), from  $1680$  to  $1650\text{ cm}^{-1}$ . Similarly, the adenine band at  $1615\text{ cm}^{-1}$  (adenine–N7) exhibited a prominent shifting to a value of  $1570\text{ cm}^{-1}$  due to strong metal complex–adenine interaction. However, no major alterations of cytosine band at  $1491\text{ cm}^{-1}$  was observed, attributed to no direct metal complex–



cytosine binding interactions. Moreover, DNA is also characterized by the spectral alterations of the PO<sub>2</sub> asymmetric and symmetric bands at ca. 1225 and 1090 cm<sup>-1</sup>, respectively which were shifted towards lower frequencies at 1232 and 1070 cm<sup>-1</sup>, respectively and were also accompanied by prominent intensity variations [54].

In case of yeast tRNA, in plane vibration bands corresponding to guanine bands at 1698 cm<sup>-1</sup> was shifted to 1688 cm<sup>-1</sup> in tRNA-**1** complex. Similarly, the band at 1660 cm<sup>-1</sup> (mainly uracil) shifted towards a lower frequency at 1655 cm<sup>-1</sup>, but the band at 1615 cm<sup>-1</sup> (mainly adenine) exhibited major upward shifting to 1633 cm<sup>-1</sup> upon complex **1**-tRNA complexation (Fig. S7b). The spectral perturbations observed for guanine, uracil, and adenine bands are indicative of complex **1** bindings to guanine and adenine N7 reactive sites (major groove) and as well as to the backbone phosphate group. Furthermore, there was no major intensity changes or shifting in the marker IR frequency bands corresponding to the ribose-phosphate vibrations at 810 and 862 cm<sup>-1</sup> and the PO<sub>2</sub> asymmetric bands at 1242 cm<sup>-1</sup>, thus it can be proposed that tRNA still remains in the A-conformational structure [55].

#### 4. Cleavage activity

##### 4.1 pBR322 cleavage studies

The DNA cleavage activity for complex **1** was analyzed by monitoring the conversion of supercoiled DNA (Form I) to the nicked circular DNA (Form II) and linear DNA (Form III). A concentration-dependent DNA cleavage was first performed to ascertain the ability of complex **1** to cleave SC DNA in absence of any reducing agent. There was a gradual decrease in the amount of Form I with a simultaneous increase in Form II (Fig. 4, Lanes 2–6) on increasing the concentration of the complex (10–30 μM). The appearance of a well-defined electrophoresis band characteristic of nicked circular form (Form II) and the absence of a band corresponding to

linear circular form (Form III) suggest that only single-strand DNA cleavage occurs for complex **1**. It was further observed that the apparent cleavage of pBR322 DNA by **1** occurred at a concentration of  $\sim 30 \mu\text{M}$  as evidenced by the disappearance of Form I and the appearance of the Form II.

Copper complexes can cleave DNA both hydrolytically and oxidatively. The interaction between metal complex and dioxygen or redox reagents are believed to be the major cause of DNA damage. In order to study the potential mechanism of DNA cleavage mediated by complex **1**, the quenching assay of pBR322 DNA were studied in the presence of some standard radical scavengers (Fig. 5). The reactions were performed under aerobic conditions by incubating **1** with DNA for 45 min in the presence of hydroxyl radical scavenger (DMSO and EtOH), singlet oxygen scavenger ( $\text{NaN}_3$ ) and superoxide scavenger (SOD). The complex did not attenuate the DNA strand scission in presence of hydroxyl radical scavengers DMSO (Fig. 5, Lanes 2) and EtOH (Lane 3) suggestive of non-involvement of diffusible ( $\cdot\text{OH}$ ) hydroxyl radicals in the cleavage mechanism. However, in the presence of SOD (Fig. 5, Lane 4), the cleavage was less significantly inhibited, which indicated that  $\text{O}_2^{\cdot-}$  might be an inhibitor in the cleavage process and reducing the amount of  $\text{O}_2^{\cdot-}$  can improve the cleavage effect. While the plasmid DNA cleavage was remarkably inhibited in the presence of singlet oxygen quencher,  $\text{NaN}_3$  (Fig. 5, Lane 5) suggesting that  $^1\text{O}_2$  is likely to be the reactive species responsible for the nuclease activity. The singlet oxygen quencher,  $\text{NaN}_3$  is a good metal-binding molecule and might simply block the complex from coordinating to DNA. Complex **1** therefore is capable of promoting DNA cleavage through an oxidative DNA damage pathway, giving active oxygen species such as singlet oxygen or singlet oxygen-like entity, probably a copper-peroxide that cleaves DNA. Based on the above results, the mechanistic pathway mediated by complex **1** involves Cu(II)

center that is initially reduced to Cu(I) species and subsequently reacts with dioxygen to form a peroxo Cu(II) derivative, which could generate ROS responsible for initiating DNA strand scission [56,57].

The preferential groove binding site of complex **1** on pBR322 was further explored in presence of the minor groove binder, DAPI and the major groove binder, methyl green. The cleavage induced by **1** was inhibited in the presence of methyl green (Fig. 5, Lane 7), suggesting the major groove binding preference for complex **1**, which is also in accordance with the conclusions inferred from the molecular docking studies.

#### 4.2. RNA cleavage studies

The ability of metal ions to promote RNA cleavage has the potential to reveal regions of the RNA molecule in close proximity to metal ions on the outer part of the folded RNA molecule. Metal ions are expected to generally promote cleavage more effective in those regions of RNA being in close proximity [58]. The electrophoresis gel pattern of RNA cleavage in presence of Cu(II) complex **1** revealed that there was little effect on RNA bands after 2 h incubation reflecting incomplete degradation of tRNA. However, as shown in Fig. 6, the cleavage pattern became more prominent on increasing the concentration (6.25–19.37  $\mu$ M) and the time of exposure of complex **1**. The cleavage was almost complete (80 to 90%) at a concentration of 19.37  $\mu$ M (Fig. 6, Lane 6) and after 10 h of incubation which showed largely diminished intensity bands of RNA. Since the cleavage rate increased as a function of incubation time and concentration, therefore it was concluded that RNA cleavage is both time and concentration dependent.

#### 4.3. Topoisomerase II inhibitory activity

DNA topoisomerases have proved to possess extraordinary clinical relevance in cancer oncology being one of the highly expressed enzymes in the cancerous cells [59]. Topo II is a validated drug target for most of the promising cancer chemotherapeutic such as the anthracyclines, acridines, and epipodophyllotoxins and the broad-spectrum of quinolone antibacterial agents. Furthermore, literature reports reveal that at high concentrations quinolone-based drugs can inhibit the catalytic DNA strand passage activity of DNA topoisomerase II [60]. The effect of concentration-dependent Topo-II inhibition assay of complex **1** was performed in the enzyme-mediated supercoiled pBR322 DNA relaxation assay in the presence of ATP using agarose gel electrophoresis. Once enzymatic activity was assayed, supercoiled plasmid DNA (SC) was converted to a relaxed circular form (R form). The relaxed circular DNA predicts that the enzyme's isomerase activity remains intact while supercoiled DNA suggests that the enzyme's action was inhibited and the appearance of linear DNA reveals the formation of permanent double strand breaks during the catalytic cycle [36]. It was observed that upon treatment with 5  $\mu$ M of complex **1** (Fig. 7, Lane 3) afforded no inhibitory activity but as the concentration reached 25  $\mu$ M (Lane 7), the complex was able to successively inhibit the DNA relaxation activity of Topo II. The observed inhibitory effect *via* binding to the ATPase domain of Topo II owing to the presence of hydrogen bonding donor and acceptor moieties which may anchor in the entrance of ATP-binding pocket and result in an increased binding affinity, thereby leading to a higher Topo-II catalytic inhibitory activity. Thus, it was concluded that **1** is a catalytic inhibitor of topoisomerases and not topoisomerase poison. Topo poisons are able to stabilize the reversible covalent Topo-DNA complex termed the 'cleavage complex' whereas Topo-II catalytic inhibitors interact non-covalently with enzyme to impede enzymatic activity during the catalytic cycle, thus, alter their normal functioning resulting in the cell death.

### 4.3. Antiproliferative studies

#### 4.3.1. Clonogenic assay

The ability of complex **1** to inhibit the growth of U2OS cancer cells has been evaluated by the clonogenic assay, which is an *in vitro* cell survival assay based on the ability of a single cell to grow into a colony. In order to evaluate the short-term growth inhibitory effect of complex **1** on exponentially growing U2OS cancer cells, these cells were treated first with increasing concentration of the complex **1** (0–30  $\mu$ M) (Fig. 8). The colony-forming cells were reduced by the complex in a dose- and time-dependent manner (Fig. 9) and no colony was observed beyond the dosage of 30  $\mu$ M. Furthermore, flow cytometry technique was used to ascertain whether inhibition of cell growth by complex **1** is due to induction of cell cycle arrest or cell death by detection of cellular DNA contents.

#### 4.3.2. Flow cytometry assay

Flow cytometry is regarded as one of the most powerful and specific methods for the integrated study of molecular and morphological events occurring during cell death and cell proliferation [61]. Generally, anticancer drugs inhibit the proliferation of cancer cell either by induction of cell cycle arrest or by apoptosis, or by the combination of both these modes. However, by measuring the DNA content, it becomes possible to identify apoptotic cells; to recognize the cell cycle phase specificity and to quantitate apoptosis. Literature reports reveal that most of the antineoplastic agents in current use arrest cell cycle either in S or G2/M phases and induce apoptotic cell death [62]. As can be seen in the Fig. 10, the untreated U2OS cells were markedly accumulated in G0/G1 phase which is the stage of active growth before DNA replication. The DNA content in S phase (26.04%) was more as compared to mitotic phase of the cell cycle (22.91%), where cell division takes place. On exposure to complex **1** (20  $\mu$ M), induction of

apoptosis and a marked S phase cell cycle arrest was observed after 48 h. The complex induced drastic accumulation of cells in S phase after the 48 h of treatment of U2OS cells along with a concomitant decrease in the G2/M phase of cell cycle which indicates that cell division has almost ceased in the presence of complex **1**. Therefore, it can be concluded that **1** inhibits the proliferation of cultured U2OS cancer cells and the growth inhibition is associated with the cell cycle arrest and induction of apoptosis; that the complex could delay or inhibit cell cycle progression through S phase arrest.

## 5. Molecular docking studies

### 5.1. Molecular docking with DNA

Molecular docking studies were performed with a purpose to ascertain the type and extent of interaction between the complex **1** and DNA/RNA. The use of molecular docking has important implications for the synthesis and development of robust drugs entities that selectively target the nucleic acids since such techniques have the potential to shed light on the interaction mode of small molecules with targets. Docking studies experiments of complex **1** and DNA duplex, d(CGCGAATTCGCG)<sub>2</sub> dodecamer (PDB ID:1BNA) results revealed that the complex **1** preferentially binds at the A–T region of the major groove of the dodecamer (Fig. 11). The major groove is rather wide and is therefore accessible to quite bulkier ligands, like proteins. Normally, electronegative A–T sequences provide better van der Waals contacts since they are narrower compared to G–C regions and therefore expose better fitting pockets for docking small flexible molecule [63]. The complex slightly bends the DNA in such a way that a part of the nalidixic acid ring moiety makes favorable stacking interactions between DNA base pairs leading to van der Waals interaction and hydrophobic contacts. Furthermore, the optimal binding conformation of the complex **1** in the A–T stretches of the major groove forms an extensive H–bonding

network (2.1–3.0 Å) between –NH<sub>2</sub> groups of DACH and C–2 carbonyl oxygen of T8 at a distance of 3.71 Å. These observations are in consistent with the DNA binding parameters obtained from the spectroscopic methods.

### 5.2. Molecular docking studies tRNA

Complex **1** was also successively docked towards the molecular target, yeast tRNA (PDB ID: 6TNA) in order to determine the preferred binding sites on tRNA. Yeast tRNA has well defined 3D structures including regions like D arm, acceptor stem, T arm,  $\psi$  loop and anticodon arm shown in Fig. 12 a and b. These structural motifs participate directly or indirectly in the targets for specific recognition process. The resulting docked model implied that complex **1** was inserted into the active pocket located between upper and lower stem and was in close proximity to U–59, U–16, U–8, A–21, A–14, C–48, C–63 and G–57 [64]. This structural feature of **1** allows it to form multiple intermolecular H–bonds between A14H2 and A21N7 of tRNA and NH<sub>2</sub> groups (H–bonding donor groups) of DACH moiety (Fig. 13). In addition these interactions are further stabilized by the van der Waal interactions.

The resulting binding energies calculated for the best docked pose of **1** with the ct–DNA and yeast tRNA targets were found to be –237 and –258 KJ mol<sup>–1</sup>, respectively. More negative binding energy value signifies greater binding propensity of a metal complex, which correlated well with our *in vitro* DNA/RNA binding experiments. Thus, it can be concluded that there is a mutual complement between spectroscopic techniques and the *in silico* studies, thereby substantiate our results.

### 5.3. Molecular docking with Topo–II

To identify the potential interaction mode of complex **1** with DNA binding site (PDB ID: 2RGR) and N–terminal domain in ATP binding site (PDB ID: 1ZXM) of Topo–II, molecular docking

simulations were carried out. The docked pose into the DNA binding site of Topo-II (Fig. 14a) revealed that complex **1** was located in the hydrophilic pocket of the enzyme and was found in close proximity to residues Asn 828, Gly 766 and Tyr 760. Additionally, **1** was found to be actively engaged in hydrogen-bonding interactions with Asn 769, which is considered an important amino acids that interact with the ligand in the DNA binding site of topoisomerase II, subsequently leading to inhibitory effect on Topo II [65].

The docking model further revealed that complex **1** was approaching towards the middle of ATP binding pocket that define the stability by strong hydrophobic interactions with Asn91, Asn95, Lys121, Gly124, Pro126 and Arg184 residues (Fig. 14b). Other hydrophobic residues such as Ile217, Ile118, Ile88 and Ala92 form a small sub pocket at the bottom of the binding site filled with water molecules that establish a hydrogen bond network connecting the side chain of Asn120 to that of Asn91. Moreover, the amino groups form hydrogen bonding interactions with Ser149, in addition to their  $\pi$ - $\pi$  interaction with aromatic ring of the complex **1** involving ATP-binding site and magnesium ion. These multiple interactions between complex **1** and residues in the ATPase domain and the magnesium ion suggest that the complex can form a strong binding interaction with Topo II, preventing the entry of ATP [66]. The resulting binding energies of docked complex with DNA binding site and ATP domain of topoisomerase II were found to be  $-264.6$  and  $-312.9$  KJ mol<sup>-1</sup>, respectively indicating better affinity towards the ATP pocket than for the DNA binding site than for the DNA binding site.

## 6. Conclusion

Nalidixic acid-DACH conjugate Cu(II) molecular entity (**1**) was synthesized, thoroughly characterized by various spectroscopic techniques (FT-IR, EPR, ESI-MS) and single crystal X-ray diffraction technique. Complex **1** was found to be a potent drug-like molecular entity in



confirmation with Lipinski rules. 1*R*, 2*R*-diaminocyclohexane ligand scaffold could reduce the drawbacks of cisplatin and its other derivatives such as toxicity etc. and nalidixic acid pharmacophore make it a suitable drug entity for selectively targeting nucleic acids. To validate our rationale, we have carried out comparative *in vitro* ct-DNA and tRNA binding studies of complex **1** by employing UV-vis, fluorescence, circular dichroism, viscosity, cyclic voltammetry, FT-IR, cleavage studies with pBR322 plasmid DNA and tRNA, respectively and molecular docking studies. The overall results of the binding studies and other experiments revealed that the complex **1** exhibited more avid binding propensity towards RNA as compared to DNA, thereby was better suited for RNA targeting. The cleavage activity of **1** on pBR322 DNA revealed significant inhibition in the cleavage pattern in presence of NaN<sub>3</sub>, suggesting an oxidative cleavage pathway involving singlet oxygen species. Furthermore, Topo-II inhibition assay was studied to unravel the mechanistic pathway of enzyme inhibitory action by **1** which suggested that the complex was catalytic inhibitor of human Topo-II at a concentration of 25  $\mu$ M. The antiproliferative activity in conjugation with FACS analysis of complex **1** was performed against U2OS bone marrow cell line to validate its potential to act as antitumor agent. The colony-forming cells were reduced by the complex in a dose- and time-dependent manner and beyond dosage of 30  $\mu$ M no colony was observed. Flow cytometry analysis of **1** against U2OS cells revealed a dramatic increase of S phase cells indicative of a delay or inhibition of cell cycle progression through S phase arrest. Additionally, molecular docking studies were also performed with molecular targets DNA, RNA and the active site of Topo-II in order to corroborate with the spectroscopic results. Therefore, complex **1** warrants further *in vitro* and *in vivo* antitumor investigations.

## 2. Experimental

### 2.1. Materials and instrumentation

Commercially obtained chemicals and solvents were used without further purification. Nalidixic acid, Ethidium Bromide (EB), 1*R*,2*R*-diaminocyclohexane (DACH), (Sigma Aldrich), copper chloride dihydrate, tris-(hydroxymethyl)aminomethane (tris-buffer) (Merck), 6X loading dye (Fermentas Life Science), human DNA topoisomerase II (Calbiochem) and Supercoiled pBR322 plasmid DNA (Genei) were utilized as received. Disodium salt of ct-DNA and yeast tRNA (Type IX from *Torula* yeast) purchased from Sigma Chem. Co. and was stored at 4 °C.

Elemental analysis was carried out on Carlo Erba Analyser Model 1106. Molar conductance was measured at room temperature on Eutech con 510 electronic conductivity bridge. Fourier-transform infrared (FT-IR) spectra were recorded on an Interspec 2020 and Spectrum Two (Pelkin Elmer) FT-IR spectrometers. The EPR spectrum of the copper complex was acquired on a Varian E 112 ESR spectrometer using X-band frequency (9.5 GHz) at liquid nitrogen temperature. ESI-MS spectrum was recorded on Micromass Quattro II triple quadrupole mass spectrometer. Electronic spectra were recorded on UV-1700 PharmaSpec UV-vis spectrophotometer (Shimadzu) in DMSO using cuvettes of 1 cm path length and data were reported in  $\lambda_{\text{max}}$ /nm. Emission spectra were made on Shimadzu RF-5301PC Spectrofluorophotometer. All the experiments involving the interaction of the complex with ct-DNA and yeast tRNA were carried out in aerated buffer (5.0 mM Tris-HCl, 50.0 mM NaCl, pH = 7.3). The concentration per base pairs for both DNA and RNA was determined spectrophotometrically by assuming  $\epsilon_{260\text{nm}}$  values to be 6600 and 7700 M<sup>-1</sup>cm<sup>-1</sup>, respectively [67,68]. The viscosity measurements were carried out using Oswald capillary viscometer maintained at 25 °C. All voltammetric experiments were performed in single compartmental cell of volume 10–15 ml containing a three-electrode system comprised of a Pt-disk working

electrode, Pt-wire as auxiliary electrode and an Ag/AgCl electrode as reference electrode. The supporting electrolyte was 0.4 M KNO<sub>3</sub> in milli-Q water. CD spectra were measured on Jasco J-815-CD spectropolarimeter at room temperature. Cleavage experiments were performed with the help of Axygen electrophoresis supported by a Genei power supply with a potential range of 50–500 V, visualized and photographed by Vilber-INFINITY gel documentation system.

## 2.2. Synthesis of [Cu(nal)<sub>2</sub>(DACH)<sub>2</sub>] (**1**)

Nalidixic acid (HnaI) (0.464 g, 2 mmol) was suspended in MeOH, and KOH (0.112 g, 2 mmol) was added to it followed by a methanolic solution of CuCl<sub>2</sub>·2H<sub>2</sub>O (0.170 g, 1 mmol). After 0.5 h of stirring a methanolic solution of 1*R*, 2*R*-diaminocyclohexane (0.228 g, 2 mmol) was added drop wise and the reaction mixture was further kept on stirring for ca. 3 h to yield a purple colored precipitate which was filtered, washed with hexane and dried under vacuum. Suitable crystals for single X-ray crystallography analysis were obtained after recrystallization from the mixture of MeOH–H<sub>2</sub>O in 8:2 ratio. (CCDC: 900311) Yield: 79%. m.p. 190 °C (dec.): Anal. Calcd. for C<sub>36</sub>H<sub>50</sub>CuN<sub>8</sub>O<sub>6</sub> (%): C, 57.32; H, 6.68; N, 14.85: Found C, 57.88; H, 6.61; N, 14.05. IR (KBr,  $\nu_{\max}/\text{cm}^{-1}$ ): 3127  $\nu(\text{--NH}_2)$ ; 2922  $\nu(\text{--CH}_2)$ ; 1632  $\nu_{\text{asym}}(\text{C=O})$ ; 1425  $\nu_{\text{sym}}(\text{C=O})$ ; 537  $\nu(\text{Cu--O})$ ; 429  $\nu(\text{Cu--N})$ .  $\Lambda_{\text{M}}$  (1 × 10<sup>−3</sup> M, DMSO): 12.00  $\Omega^{-1} \text{ cm}^2 \text{ mol}^{-1}$  (non-electrolyte). UV-vis (1 × 10<sup>−3</sup> M DMSO,  $\lambda_{\text{nm}}$ ): 263, 328, 630. ESI-MS (*m/z*): 755.1 [C<sub>36</sub>H<sub>50</sub>CuN<sub>8</sub>O<sub>6</sub> + H]<sup>+</sup>.

## 2.3. Description of X-ray Crystal structure

Suitable X-ray quality crystals of the complex **1** were obtained after slow evaporation of the reaction mixture at room temperature. Single crystal X-ray structural studies of complex was performed on a CCD Oxford Diffraction Xcalibur Saphir 3 diffractometer employing graphite-monochromated Mo-K $\alpha$  radiation generated from a fine-focus sealed tube ( $\lambda = 0.71073 \text{ \AA}$ ) at 140(2) K. Data collection strategy was evaluated by using the CrysAlisPro CCD software.

Collections of data were observed by the standard  $\omega$  scan techniques and were scaled and reduced using CrysAlisPro RED software. The structure was solved by direct methods using SIR-97 [69] and refined by least-squares methods on  $F^2$  using SHELXL-97 [70]. The positions of all atoms were obtained by direct methods. Anisotropic thermal parameter were assigned to all non-hydrogen atoms and the remaining hydrogen atoms were placed in geometrically constrained position and refined as riding atoms with a common fixed isotropic thermal parameter. The drawing of the complex was realized with PLATON [71]. A summary of the selected crystallographic information is given in Table 1.

#### *2.4. In vitro DNA/RNA binding and cleavage experiments*

DNA binding experiments include absorption spectral traces, emission spectroscopy, viscosity measurements and CD conformed to the standard methods and practices previously adopted by our laboratory [72–74]. The cleavage experiments of supercoiled pBR322 DNA (300 ng) by complex **1** in Tris-HCl/NaCl (5:50 mM) buffer at pH 7.2 was carried out using agarose gel electrophoresis. The samples were incubated for 45 min at 37 °C and cleavage process with and without ROS was monitored using agarose gel electrophoresis. A loading buffer containing 25% bromophenol blue, 0.25% xylene cyanol, 30% glycerol was added and electrophoresis was carried out at 50 V for 1 h in Tris-HCl buffer using 1% agarose gel containing 1.0 mg/ml ethidium bromide.

RNA binding studies were performed in Tris-HCl/NaCl (5:50 mM) buffer at pH 7.2 which includes absorption titration, emission spectroscopy and CD measurement according to the protocol described previously [75]. While measuring the absorption spectra an equal amount of DNA/RNA was added to both the compound solution and the reference solution to eliminate the absorbance of the ct-DNA/tRNA itself, and absorbance of the Tris buffer was subtracted through

base line correction. The RNA cleavage reaction was performed in a Tris–HCl 40 mM, pH 8.0 buffer. The reaction mixture containing increasing concentration of complex **1** was incubated for 8 h at 37 °C. The electrophoresis was performed using Tris–Borate–EDTA buffer (TBE) for 200 min at 50 V/cm. The gel was then soaked 20 min with and rinsed 30 min in distilled water. RNA fragments were visualized, after an incubation with EB (0.5 mg/mL), using an UV transilluminator.

### 2.5. Topoisomerase II inhibition assay

DNA topoisomerase II $\alpha$  (Topo II) was purchased from Sigma and no further purification was performed. One unit of the enzyme was defined as completely relax 0.3  $\mu$ g of negatively supercoiled pBR322 DNA in 15 min at 37 °C under the standard assay conditions. The reaction mixture (30.0  $\mu$ L) contained 10.0 mM Tris–HCl (pH 7.9), 50.0 mM NaCl, 50.0 mM KCl, 5.0 mM MgCl<sub>2</sub>, 0.1 mM Na<sub>2</sub>H<sub>2</sub>edta, 15.0  $\mu$ g/mL BSA, 1.0 mM ATP, 0.25  $\mu$ g pBR322 DNA, 5 Unit Topo II, and complex **1**. The samples were electrophoresed through 1% agarose in TBE at 50 V for 8 h.

### 2.6. Molecular docking studies

The rigid molecular docking studies were performed by using HEX 6.1 software, [76] which is an interactive molecular graphics program for calculating and displaying feasible docking modes of an enzymes and DNA molecule. Structure of the complex **1** was converted it into PDB format from mol format by OPENBABEL (<http://www.vcclab.org/lab/babel/>). The crystal structure of the B–DNA dodecamer d(CGCGAATTCGCG)<sub>2</sub> (PDB ID: 1BNA), RNA (PDB ID: 6TNA) and human–DNA–Topo–II (PDB ID: 1ZXN, 2RGR) were downloaded from the protein data bank (<http://www.rcsb.org/pdb>). Visualization of the docked position has been done by using

CHIMERA ([www.cgl.ucsf.edu/chimera](http://www.cgl.ucsf.edu/chimera)) and PyMol (<http://pymol.sourceforge.net/>) molecular graphics program.

## 2.7. Antiproliferative Studies

### 2.7.1. Cell lines and culture conditions.

Human osteoblastoma cell line, U2OS was used for the present study. U2OS cell line was obtained from National Center for Cell Science, Pune, India. Cells were cultured in DMEM (GIBCO, USA) containing 10% FBS (GIBCO, USA), 100 U of Penicillin G/ml and 100 mg of streptomycin/ml (Invitrogen, USA) at 37 °C in a humidified atmosphere containing 5% CO<sub>2</sub>.

### 2.7.2. Cell cycle analysis by PI staining.

Complex 1–induced cell cycle effects were analyzed by flow cytometry after DNA staining with propidium iodide (PI) according to Nicoletti et al. [77]. Briefly, Cells were grown in 35 mm dishes at a density of  $2 \times 10^5$  cells/dish. At 60% confluence, cells were treated with complex 1 for 72 h. Cells were fixed in 70% ethanol overnight at –20 °C and were collected by trypsinization before staining with propidium iodide (PI; 20 µg/ml in PBS containing 0.1% Triton X–100 and 0.2 mg/ml RNase A) for 30 min at 37 °C. Cells were then analyzed by Accuri C6 flow cytometer (BD Biosciences) using FlowJo Data analysis software to determine the stages of the cell cycle.

## Acknowledgements

The authors are grateful to SAIF Panjab University, Chandigarh, STIC Cochin University, Cochin and IIT Bombay, Mumbai, for providing ESI–MS, elemental analysis facility, and EPR measurements respectively. The author (I. Yousuf) expresses his gratitude to *University Grants Commission* (UGC), New Delhi, for Junior Research Fellowship.

## Appendix A. Supplementary data

Supplementary data associated with to this article can be found, in the online version.

Crystallographic data is also available from the CCDC as file CCDC 900311.

## References

- [1] L. Kelland, *Nat. Rev. Cancer* 7 (2007) 573–584.
- [2] S. H. van Rijt, P. J. Sadler, *Drug Discov. Today* 14 (2009) 1089–1097.
- [3] S. van Zutphen, J. Reedijk, *Coord. Chem. Rev.* 249 (2005) 2845–2853
- [4] S.P. Fricker, *Dalton Trans.* 43 (2007) 4903–4917.
- [5] L. Ronconi, P.J. Sadler, *Coord. Chem. Rev.* 251 (2007) 1633–1648.
- [6] G. Gasser, I. Ott, N. Metzler–Nolte *J. Med. Chem.* 54 (2011) 3–25.
- [7] N. Foloppe, N. Matassova, F. Aboul–ela, *Drug Discov. Today* 11 (2006) 1019–1027.
- [8] C.S Chow, F.M. Bogdan, *Chem. Rev.* 97 (1997) 1489–1512.
- [9] (a) P.A. Sharp, *Cell* 136 (2009) 577–580; Y. Tor, *ChemBioChem.* 4 (2003) 998–1007;  
(b) W.E. Georgiannaa, D.D. Young, *Org. Biomol. Chem.* 9 (2011) 7969–7978.
- [10] L. Guan, M.D. Disney, *ACS Chem. Biol.* 7 (2012) 73–86.
- [11] D. I. Bryson, W. Zhang, P. M. McLendon, T. M. Reineke, W. L. Santos, *ACS. Chem. Biol.* 7 (2012) 210–217.
- [12] A. Grau–Campistany, A. Massaguer, D. Carrion–Salip, F. Barragan, G. Artigas, P. Lopez–Senin, V. Moreno, V. Marchan, *Mol. Pharmaceutics* 10 (2013) 1964–1976.
- [13] J. Boer, K.F. Blount, W. Luedtke, L. Elson–Schwab, Y.T. *Angew. Chem. Int. Ed.* 44 (2005) 927–932.
- [14] D. P. Buck, C.B. Spillane, J.G. Collins, F.R. Keene, *Mol. Biosyst.*, 4 (2008) 851–854.
- [15] K. Gumireddy, D.D. Young, X. Xiong, J.B. Hogenesch, Q. Huang, A. Deiters, *Angew. Chem. Int. Ed.* 47 (2008) 7482–7484.
- [16] J.C. Henry, A.C.P. Azevedo–Pouly, T.D. Schmittgen. *Pharm. Res.* 28 (2011) 3030–3042.
- [17] A.L. Barry, R.N. Jones, C. Thornsberry, L.W. Ayers, E.H. Gerlach, H.M. Sommers, *Antimicrob. Agents Chemother.* 25 (1984) 633–637.

- [18] K. Akahane, M. Sekiguchi, T. Une, Y. Osadaanti, *Antimicrob. Agents Chemother.* 33 (1989) 1704–1708.
- [19] R. Hudej, J. Kljun, W. Kandioller, U. Repnik, B. Turk, C.G. Hartinger, B.K. Keppler, D. Miklavcic, I. Turel, *Organometallics* 31 (2012) 5867–5874.
- [20] J. Kljun, I. Bratsos, E. Alessio, G. Psomas, U. Repnik, M. Butinar, B. Turk, I. Turel, *Inorg. Chem.* 52 (2013) 9039–9052.
- [21] S.S. Lee, Ok–Sang Jung, C.O. Lee, S.U. Choi, M.–J. Jun, Y.S. Sohn, *Inorg. Chim. Acta* 239 (1995) 133–138.
- [22] J. Kljun, A. K. Bytze, W. Kandioller, C. Bartel, M.A. Jakupec, C.G. Hartinger, B.K. Keppler, I. Turel, *Organometallics* 30 (2011) 2506–2512.
- [23] N.B. Behrens, G. Mendoza–Diaz, *Inorg. Chim. Acta* 125 (1986) 21–26.
- [24] G. Mendoza–Diaz, J. Ireta–Moreno, J. *Inorg. Biochem.* 54 (1994) 235–246.
- [25] G. Mendoza–Diaz, L.M.R. Martinez–Aguilera, R. Perez–Alonso, *Inorg. Chim. Acta* 138 (1987) 41–47.
- [26] G. Psomas, D.P. Kessissoglou, *Dalton Trans.* 42 (2013) 6252–6276.
- [27] E.Wong, C.M. Giandomenico, *Chem. Rev.* 99 (1999) 2451–2466.
- [28] A. Prisecaru, V. McKee, O. Howe, G. Rochford, M. McCann, J. Colleran, M. Pour, N. Barron, N. Gathergood, A. Kellett. *J. Med. Chm.* 56 (2013) 8599–8615.
- [29] C. Sissi, F. Mancin, M. Gatos, M. Palumbo, P. Tecilla, U. Tonellato, *Inorg. Chem.*, 44 (2005) 2310–2317.
- [30] C. Santini, M. Pellei, V. Gandin, M. Porchia, F. Tisato, C. Marzano, *Chem. Rev.* 2014, 114, 815–862.



- [31] S. Roy, P. Uma. Maheswari, M. Lutz, A.L. Spek, H. den Dulk, S. Barends, G.P. van Wezel, F. Sek Hartl, J. Reedijk, *Dalton Trans.* (2009) 10846–10860.
- [32] C. Marzano, M. Pellei, F. Tisato, C. Santini, *Anti-cancer Agents Med. Chem.* 9 (2009) 185–210.
- [33] S. Tardito, I. Bassanetti, C. Bignardi, L. Elviri, M. Tegoni, C. Mucchino, O. Bussolati, R. Franchi–Gazzola, L. Marchi, *J. Am. Chem. Soc.* 133 (2011) 6235–6242.
- [34] F. Arjmand, M. Muddassir, Y. Zaidi, D. Ray, *Med. Chem. Commun.* 4 (2013) 394–405.
- [35] F. Liu, *Annu. Rev. Biochem.* 58 (1989) 351–375.
- [36] K. Suzuki, F. Shono, M. Uyeda, *Biosci. Biotechnol. Biochem.* 66 (2002) 1706–1712.
- [37] V. Karthick, K. Ramanathan, V. Shanthi, R. Rajasekaran, *Cell Biochem. Biophys.* 66 (2013) 657–669.
- [38] C.D. Samara, G. Tsotsou, L.V. Ekateriniadou, A.H. Kortsaris, C.P. Raptopoulou, A. Terzis, D.A. Kyriakidis, D.P. Kessissoglou, *J. Inorg. Biochem.* 71 (1998) 171–179.
- [39] B.J. Hathaway, D.E. Billing, *Coord. Chem. Rev.* 5 (1970) 143–207.
- [40] I.A. Koval, M. Sgobba, M. Huisman, M. Luken, E. Saint–Aman, P. Gamez, B. Krebs J. Reedijk, *Inorg. Chim. Acta* 359 (2006) 4071–4078.
- [41] X. Liang, X. Zou, L. Tan, W. Zhu, *J. Inorg. Biochem.* 104 (2010) 1259–1266.
- [42] F. Zhang, Q.–q. Zhang, W.–g. Wang, X.–l. Wang, *J. Photochem. Photobiol. A: Chem.* 184 (2006) 241–249.
- [43] E.F. Healy, *J. Chem. Educ.* 84 (2007) 1304–1307.
- [44] N.W. Luedtke, J.S. Hwang, E. Nava, D. Gut, M. Kol, Y. Tor, *Nucl. Acids Res.* 31 (2003) 5732–5740.
- [45] B.K. Paul, N. Guchhait, *J. Phys. Chem. B* 115 (2011) 11938–11949.

- [46] F. Arjmand, S. Parveen, D.K. Mohapatra, *Inorg. Chim. Acta* 388 (2012) 1–10.
- [47] M. Vorlickova, *Biophys. J.* 69 (1995) 2033–2043.
- [48] J. Kypr, M. Vorlickova, *Biopolymers* 67 (2002) 275–277.
- [59] E. Froehlich, J.S. Mandeville, D. Arnold, L. Kreplak, H.A. Tajmir-Riahi, *Biomacromolecules* 13 (2012) 282–287.
- [50] J.M. Kelly, A.B. Tossi, D.J. McConnell, C. OhUigin, *Nucl. Acids Res.* 13 (1985) 6017–6034.
- [51] H. Xu, Y. Liang, P. Zhang, F. Du, B.–R. Zhou, J. Wu, J.–H. Liu, Z.–G. Liu, L.–N. Ji, *J. Biol. Inorg. Chem.* 10 (2005) 529–538.
- [52] T. Hirohama, Y. Kuranuki, E. Ebina, T. Sugizaki, H. Arai, M. Chikira, P.T. Selvi, M. Palaniandavar, *J. Inorg. Biochem.* 99 (2005) 1205–1219.
- [53] M.T. Carter, M. Rodriguez, A.J. Bard, *J. Am. Chem. Soc.* 111 (1989) 8901–8911.
- [54] F. Arjmand, M. Muddassir, *J. Photochem. Photobiol. B Biol.* 101 (2010) 37–46.
- [55] H. Arakawa, J.F. Neault, H.A. Tajmir-Riahi, *Biophys. J.* 81 (2001) 1580–1587.
- [56] D.–Dong Li, J.–Lei Tian, Wen Gu, Xin Liu, H.–Hui Zeng, S.–Ping Yan, *J. Inorg. Biochem.* 105 (2011) 894–901.
- [57] G.–Ying Li, K.–Jie Du, J.–Quan Wang, J.–Wen Liang, J.–Feng Kou, X.–Juan Hou, Liang–Nian Ji, Hui Chao, *J. Inorg. Biochem.* 119 (2013) 43–53.
- [58] M. Forconi, D. Herschlag, *Methods Enzymol.* 468 (2009) 91–106.
- [59] D. Jayaraju, A.K. Kondapi, *Curr. Sci.* 81 (2001) 787–792.
- [60] M.J. Robinson, B.A. Martin, T.D. Gootz, P.R. McGuirk, M. Moynihan, J.A. Sutcliffe, N. Osheroff, *J. Biol. Chem.* 266 (1991) 14585–14592.

- [61] H.Y. Shrivastava, T. Ravikumar, N. Shanmugasundaram, M. Babub, B.U. Nair, *Free Radical Bio. Med.* 38 (2005) 58–69.
- [62] C.–Y. Gao, X. Qiao, Z.–Y. Ma, Z.–G. Wang, J. Lu, J.–L. Tian, J.–Y. Xu, S.–P. Yan, *Dalton Trans.* 41 (2012) 12220–12232.
- [63] B.K. Sahoo, K.S. Ghosh, R. Bera, S. Dasgupta, *Chem. Phys.* 351 (2008) 163–169.
- [64] D. Agudelo, P. Bourassa, M. Beauregard, G. Berube, H.–A. Tajmir–Riahi, *Plos one* 8 (2013) e69248.
- [65] P. Furet, J. Schoepfer, T. Radimerski, P. Chène, *Bioorg. Med. Chem. Letters* 19 (2009) 4014–4017.
- [66] C.–X. Hu, Z.–L. Zuo, B. Xiong, J.–G. Ma, M.–Y. Geng, L.–P. Lin, H.–L. Jiang, J. Ding, *Mol. Pharmacol.* 70 (2006) 1593–1601.
- [67] M.E. Reicmann, S.A. Rice, C.A. Thomas, P. Doty, *J. Am. Chem. Soc.* 76 (1954) 3047–3053.
- [68] K.A. Meadows, F. Liu, J. Sou, B.P. Hudson, D.R. McMillin, *Inorg. Chem.* 12 (1991) 2919–2923.
- [69] A. Altomare, M.C. Burla, M. Camalli, G.L. Cascarano, C. Giocavazzo, A. Guagliardi, A.G.C. Moliterni, G. Polidori, S. Spagna, *J. Appl. Crystallogr.* 32 (1999) 115–119.
- [70] G.M. Sheldrick, *SHELX–97*, Program for Crystal Structure refinement, University of Göttingen, Germany, 1997.
- [71] A.L. Spek, *PLATON Procedure*, A multipurpose Crystallographic Tool, Utrecht University, Utrecht, The Netherlands, 1998.
- [72] J.R. Lakowicz, G. Webber, *Biochemistry* 12 (1973) 4161–4170.
- [73] A. Wolfe, G.H. Shimer Jr., T. Meehan, *Biochemistry* 26 (1987) 6392–6396.

- [74] F. Arjmand, S. Parveen, M. Afzal, L. Toupet, T. B. Hadda, *Eur. J. Med. Chem.* 49 (2012) 1–10.
- [75] M. Marketaki, E. Touloupakis, G. Charalambidis, M.–C. Chalbot, D.F. Ghanotakis and A.G. Coutsolelos, *J. Porphyrins Phthalocyanines* 16 (2012) 1–9.
- [76] D. Mustard, D.W. Ritchie, *Proteins: Struct., Funct., Bioinf.* 60 (2005) 269–274.
- [77] I. Nicoletti, G. Migliorati, M.C. Pagliacci, F. Grignani, C. Riccardi, *J. Immunol. Methods* 139 (1991) 271–279.

### Figure Captions

**Fig.1.** (a) Molecular structure of complex **1** with partial labeling. (b) Intermolecular hydrogen bonded 1D polymeric array along a axis in complex **1**. Hydrogen atoms have been omitted for clarity.

**Fig.2.** Absorption spectral traces of complex **1** in 5mM Tris HCl/50 mM NaCl buffer at pH 7.2 upon addition of (a) ct–DNA and (b) yeast tRNA at 25 °C. Inset: Plots of  $[\text{DNA or RNA}]/\epsilon_a - \epsilon_f$  ( $\text{M}^2\text{cm}$ ) vs.  $[\text{DNA or RNA}]$  for the titration with complex **1**, ▲ experimental data points, full lines, linear fitting of the data.  $[\text{DNA}], [\text{RNA}] = 0.00\text{--}5.00 \times 10^{-5} \text{ M}$ ,  $[\text{Complex } \mathbf{1}] = 1.0 \times 10^{-5} \text{ M}$ .

**Fig.3.** Emission spectra of complex **1** in Tris–HCl buffer at pH 7.2 upon addition (a) ct–DNA and (b) yeast tRNA  $[\text{DNA}], [\text{RNA}] = 0.00\text{--}3.69 \times 10^{-5} \text{ M}$ ,  $[\text{Complex } \mathbf{1}] = 1.67 \times 10^{-5} \text{ M}$  at 25 °C. Arrow shows change in intensity with increasing concentration of DNA/RNA.

**Fig.4.** Agarose gel electrophoresis showing cleavage of pBR322 supercoiled DNA (300 ng) by complex **1** at 37 °C after 45 min of incubation at different concentrations; Lane 1, DNA control; Lane 2, 10  $\mu\text{M}$  of **1** + DNA; Lane 3, 15  $\mu\text{M}$  of **1** + DNA; Lane 4, 20  $\mu\text{M}$  of **1** + DNA; Lane 5, 25  $\mu\text{M}$  of **1** + DNA; Lane 6, 30  $\mu\text{M}$  of **1** + DNA.

**Fig.5.** Agarose gel electrophoresis showing cleavage of pBR322 supercoiled DNA (300 ng) by complex **1** (30  $\mu$ M) at 37 °C after 45 min of incubation in presence of different ROS and groove binding agents. Lane 1, DNA control; Lane 2, **1** + DMSO (0.4 mM) + DNA; Lane 3, **1** + Ethyl alcohol (0.4 mM) + DNA; Lane 4, **1** + SOD (0.25 mM) + DNA; Lane 5, **1** + sodium azide (0.4 mM) + DNA; Lane 6, **1** + DNA + DAPI (8  $\mu$ M); Lane 7, **1** + DNA + Methyl green (2.5  $\mu$ M of a 0.01 mg/ml solution).

**Fig.6.** Agarose gel electrophoresis showing RNA cleavage in buffer after 8 h of incubation time at 37 °C with increasing concentrations of complex **1** in a TBE 40 mM, pH 8.0 buffer, 30 mL of yeast tRNA solution ( $3 \times 10^{-3}$  M). Lane 1: RNA control; Lane 2: 6.25  $\mu$ M of **1** + RNA; Lane 3: 9.25  $\mu$ M of **1** + RNA; Lane 4: 12.37  $\mu$ M of **1** + RNA; Lane 5: 15.87  $\mu$ M of **1** + RNA; Lane 6: 19.37  $\mu$ M of **1** + RNA.

**Fig.7.** Agarose gel electrophoresis showing effect of different concentrations of complex **1** on the activity of human–DNA Topo II $\alpha$  (Topo–II, 5 units); Lane 1: DNA control; Lane 2: Topo–II control (Topo–II + DNA); Lane 3: 5  $\mu$ M of **1** + DNA + Topo–II; Lane 4: 10  $\mu$ M of **1** + DNA + Topo–II; Lane 5: 15  $\mu$ M of **1** + DNA + Topo–II; Lane 6: 20  $\mu$ M of **1** + DNA + Topo–II; Lane 7: 25  $\mu$ M of **1** + DNA.

**Fig.8.** Clonogenic assay in U2OS cells exposed to varying concentration of complex **1** for 48 h.

**Fig.9.** Dose– and time– dependent effects of complex **1** on cell viability in U2OS cells.

**Fig.10.** Cell cycle distribution analyzed by flow cytometry in a time dependent manner upon treatment with complex **1** (20  $\mu$ M) and the corresponding DMSO control.

**Fig.11.** Molecular docked model of complex **1** fitted into A–T region of the major groove of DNA dodecamer duplex of sequence d(CGCGAATTCGCG)<sub>2</sub>.

**Fig. 12.** Structure of tRNA<sup>Phe</sup> (a) Cloverleaf model and (b) 3–Dimensional model.

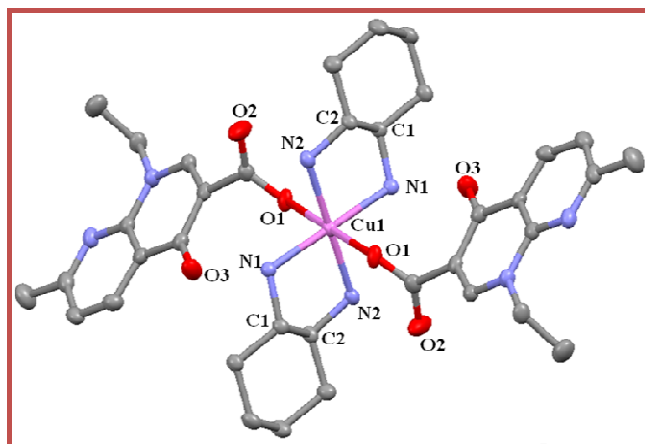
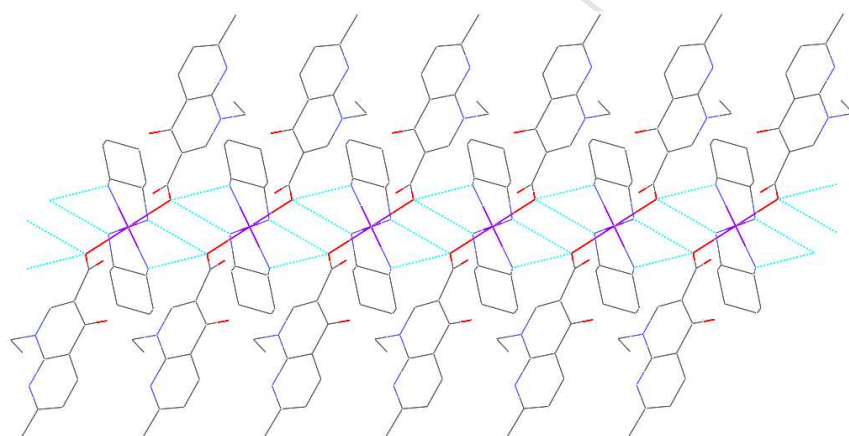
**Fig.13.** Docking structure between complex **1** and yeast tRNA (PDB ID: 6TNA).

**Fig.14.** Molecular docked model of complex **1** with the human–DNA–Topo II $\alpha$  (a) DNA binding site of Topo II $\alpha$  (PDB ID: 2RGR) (b) ATP binding pocket of human Topo II $\alpha$  parallel to the Mg<sup>+2</sup> ion (PDB ID: 1ZXN). The ATP-binding domain is shown in a cartoon view.

**Table 1:** Selected Crystallographic data for the complex **1**.

Parameter	
Empirical formula	C <sub>36</sub> H <sub>50</sub> Cu N <sub>8</sub> O <sub>6</sub>
Formula weight (g mol <sup>-1</sup> )	754.39
Crystal system	Triclinic
Space group	<i>P</i> -1.
a (Å)	5.2230(2)
b (Å)	12.4475(7)
c (Å)	16.6946(8)
α (deg)	110.839(5)°
β (deg)	94.002(4)°
γ (deg)	90.417(4)°
V(Å <sup>3</sup> )	1011.30(8)
Z	1
D <sub>calc</sub> (Mg m <sup>-3</sup> )	1.239
μ (mm <sup>-1</sup> )	0.591
F(000)	399.0
Crystal size (mm)	0.289 x 0.162 x 0.105
Temp (K)	140 K
Measured reflections	8653
Unique reflections	3607
θ range (deg)/ completeness (%)	3.27 to 27.00
No. of data/parameters/restraints	4386 / 0 / 232
GoF <sup>a</sup>	1.105
R <sup>b</sup> [I>2σ(I)]	0.0396
wR <sub>2</sub> <sup>b</sup> (all data)	0.1301
Largest diff. peak/hole (e.Å <sup>-3</sup> )	0.432/-0.279

<sup>a</sup>GoF is defined as  $\{\sum[w(F_o^2 - F_c^2)]/(n-P)\}^{1/2}$  where  $n$  is the number of data and  $p$  is the number of parameters. <sup>b</sup>R =  $\{\sum||F_o| - |F_c||/\sum|F_o|, wR^2 = \{\sum w(F_o^2 - F_c^2)^2 / \sum w(F_o^2)^2\}^{1/2}$ .

**Figures****Fig. 1a****Fig. 1b**



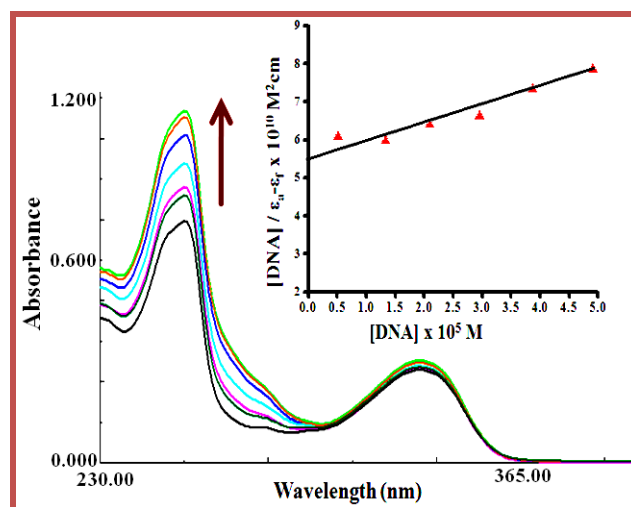


Fig. 2a

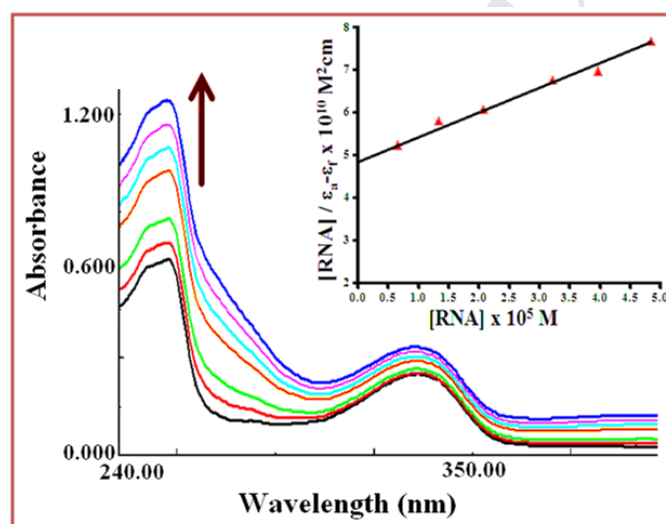


Fig. 2b

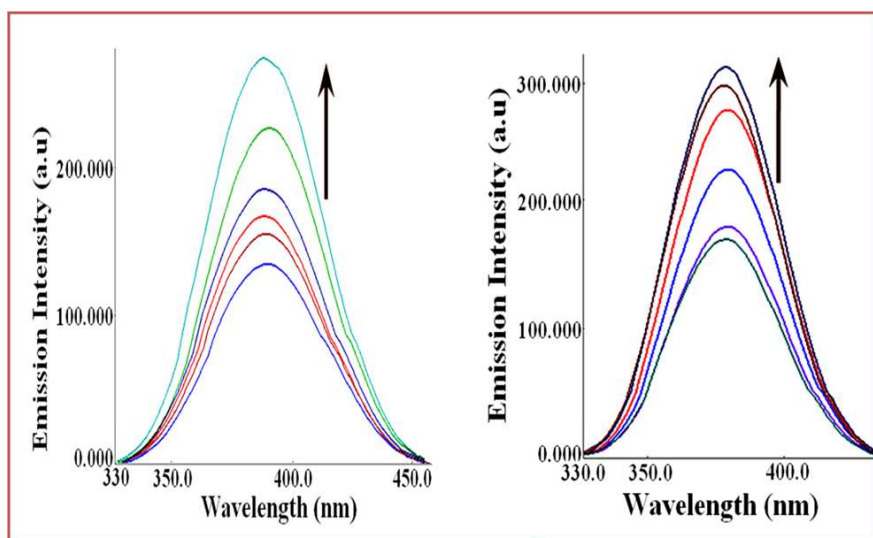


Fig. 3

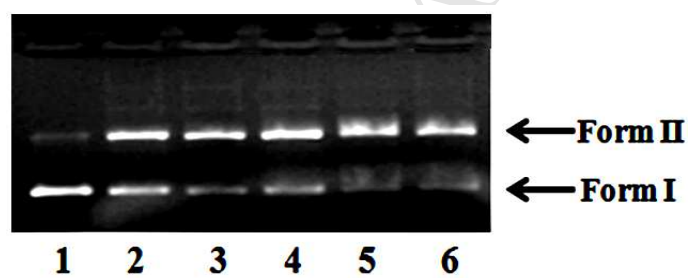


Fig. 4

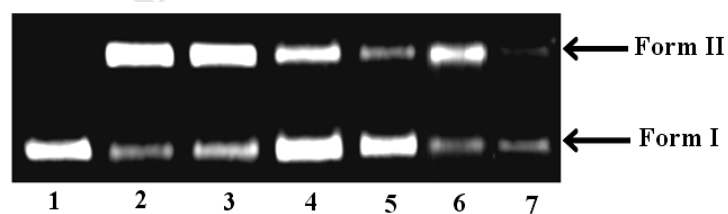


Fig. 5

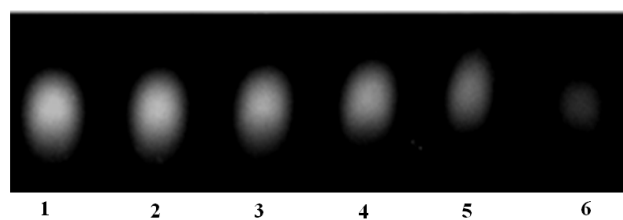


Fig. 6

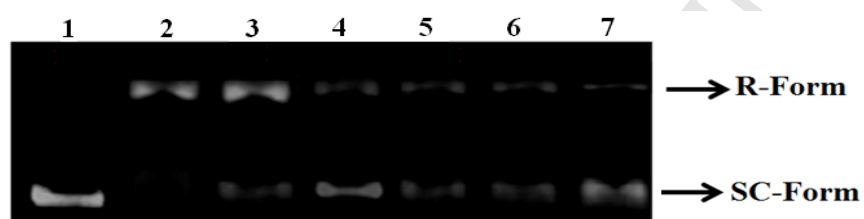


Fig. 7

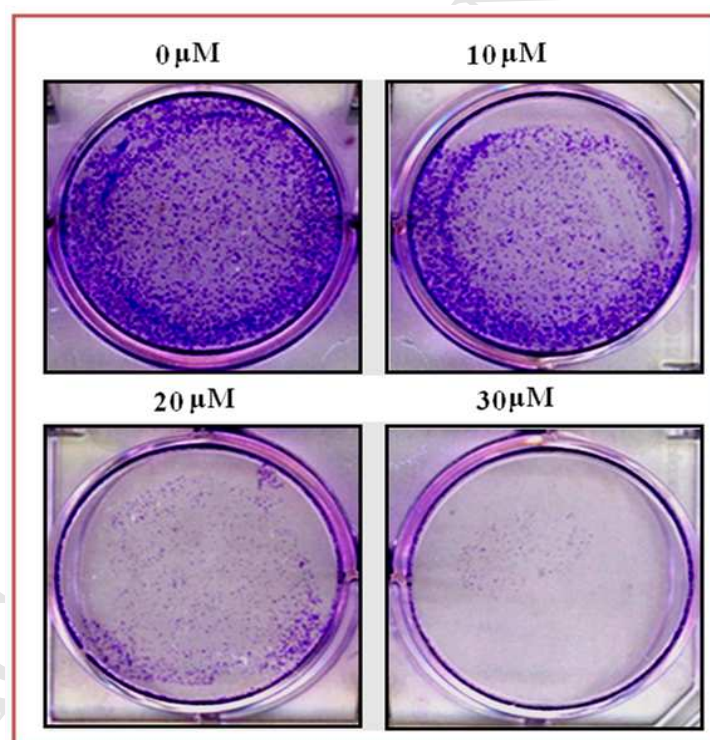


Fig. 8

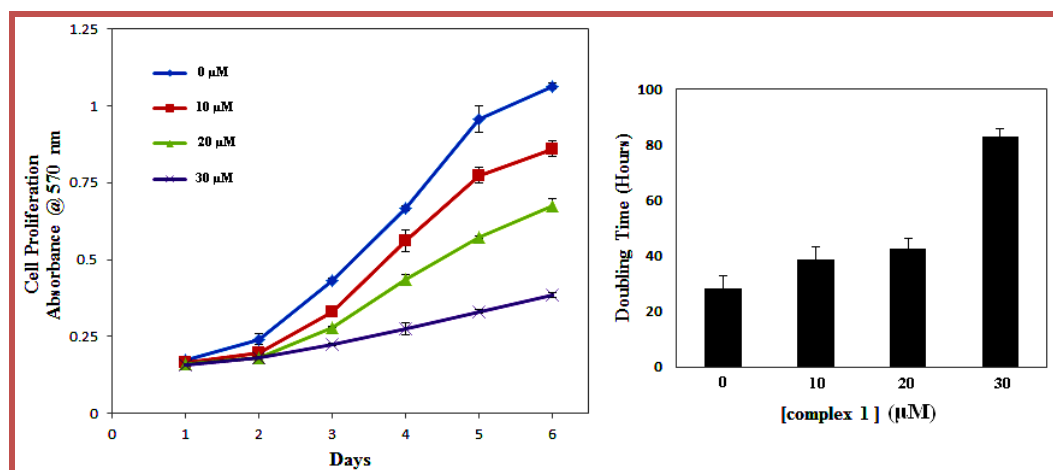


Fig. 9

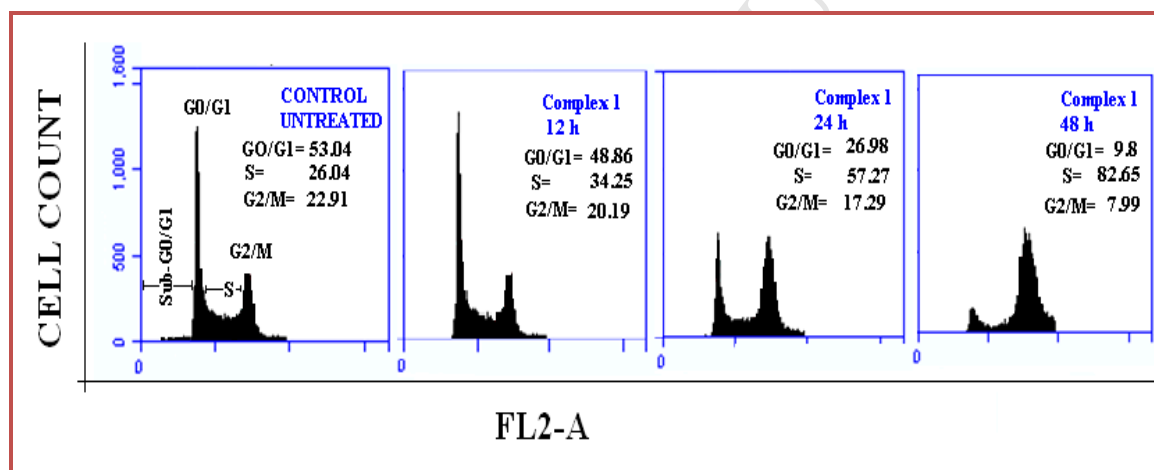


Fig. 10

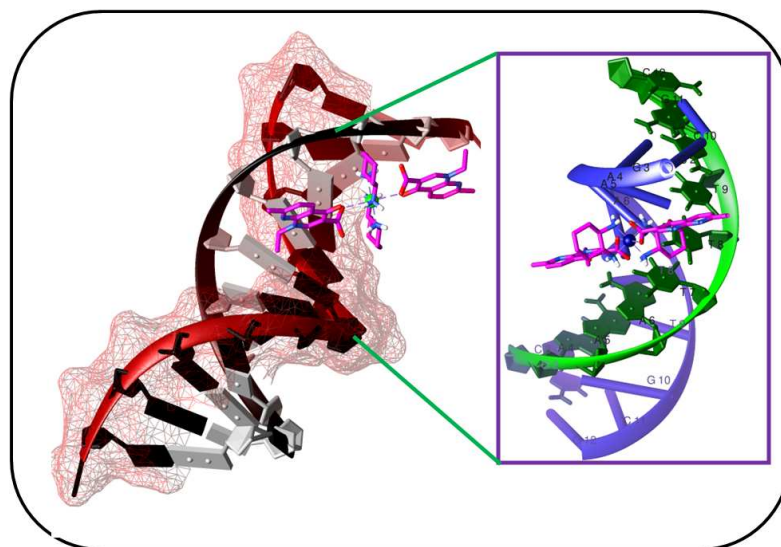


Fig. 11

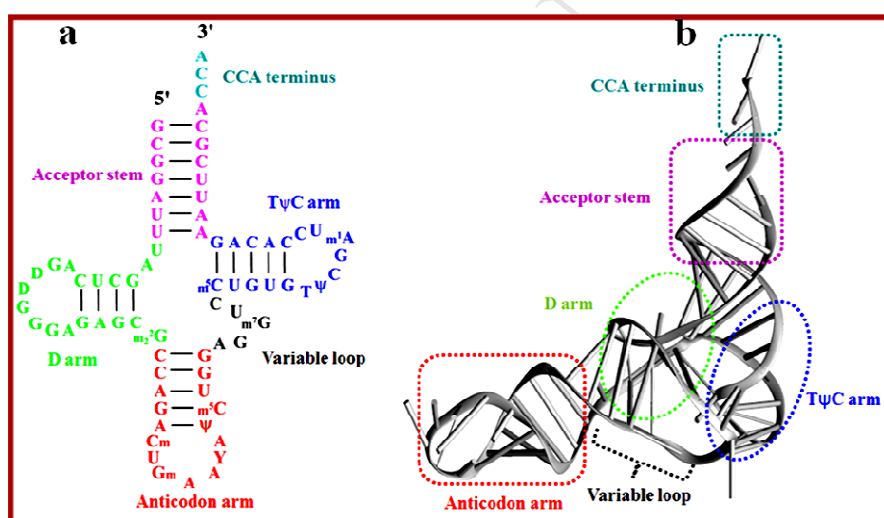


Fig. 12

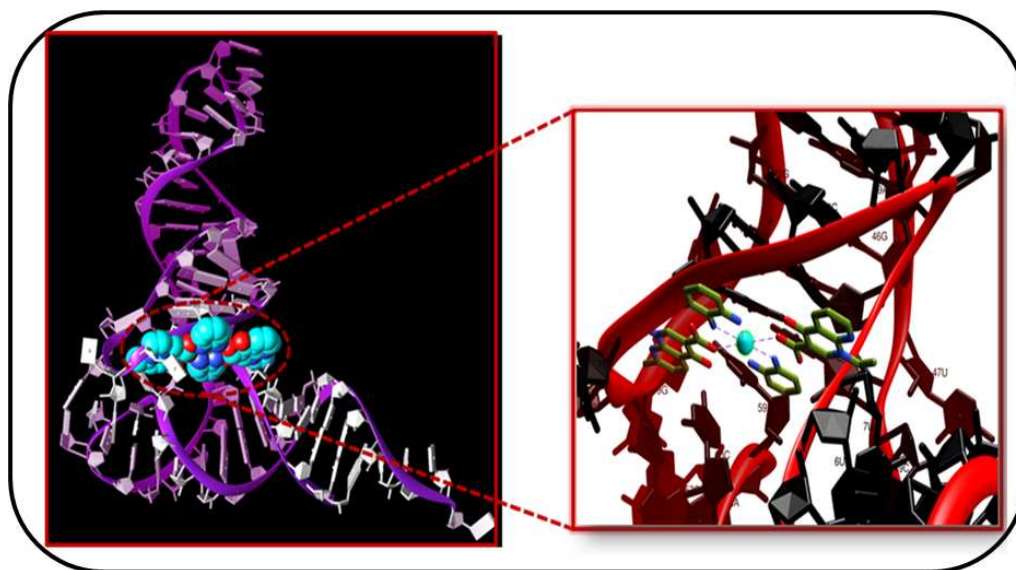


Fig.13

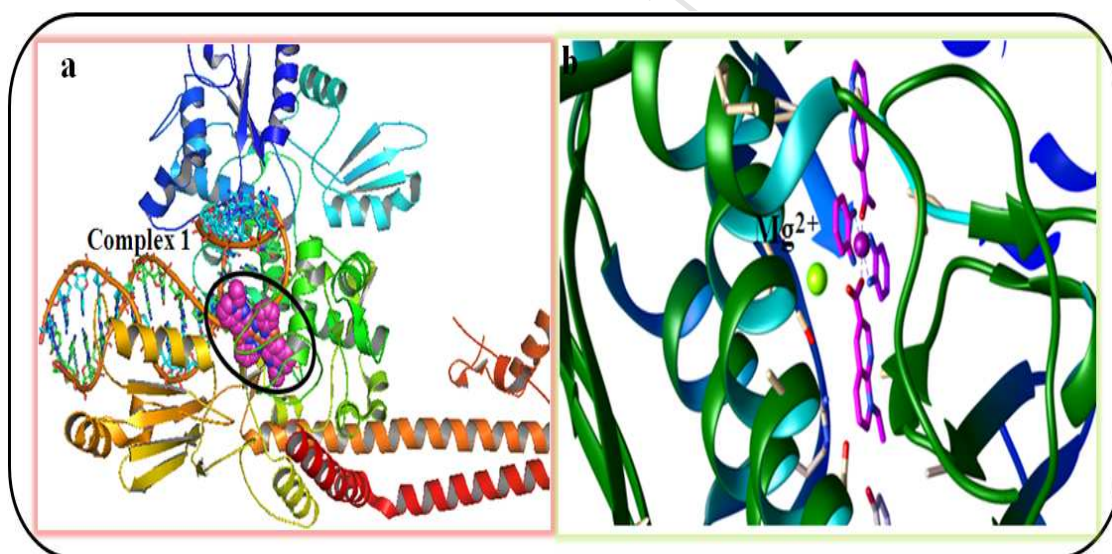
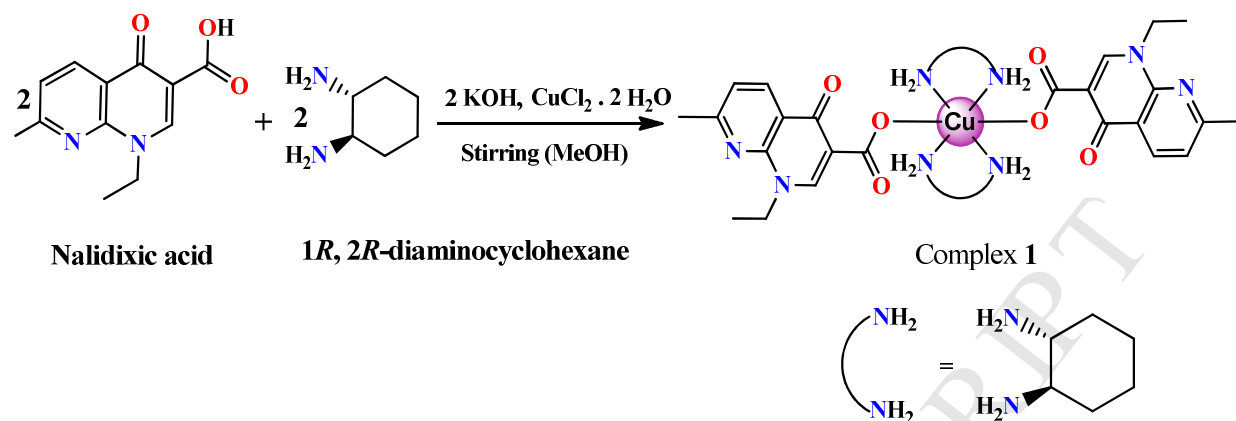


Fig.14



**Scheme 1.** Synthetic route for complex **1**.

### Research Highlights

- Copper based drug entity, **1** was synthesized from nalidixic acid and DACH ligands.
- Complex **1** showed avid binding propensity for tRNA as compared to DNA.
- Complex **1** was found to be a catalytic inhibitor of human Topo–II.
- Antiproliferative activity and flow cytometry suggested S phase cell cycle arrest.
- Molecular docking results corroborated well with other spectroscopic results.



## Supplementary information

**Synthesis, crystal structure and antiproliferative activity of Cu(II) nalidixic acid–DACH conjugate: Comparative *in vitro* DNA/RNA binding profile, cleavage activity and molecular docking studies**

**Farukh Arjmand<sup>\*,a</sup>, Imtiyaz Yousuf<sup>a</sup>, Taibi ben Hadda<sup>b</sup>, Loic Toupet<sup>c</sup>**

<sup>a</sup> Department of Chemistry, Aligarh Muslim University, Aligarh 202002, Uttar Pradesh, India.

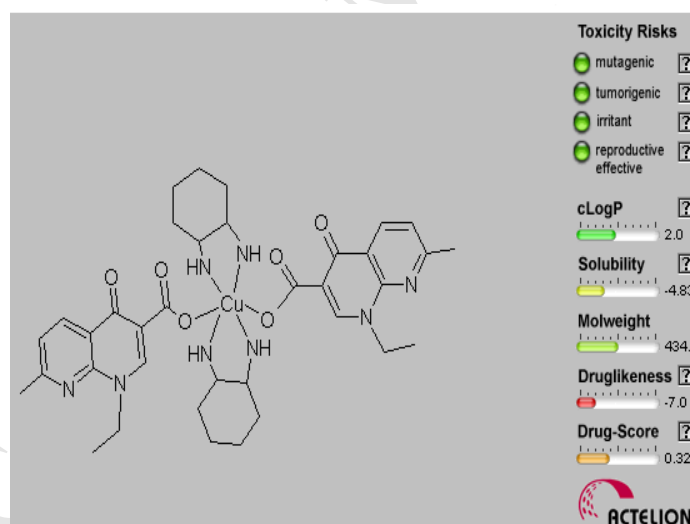
<sup>b</sup> Laboratoire Chimie des Matériaux, FSO, Université Mohammed I, Oujda 60000, Morocco.

<sup>c</sup> Institut de Physique de Rennes, UMR 625, Université de Rennes 1, Campus de Beaulieu Bat. 11 A, 263 av. Général Leclerc, 35042 Rennes Cedex, France.

\*Corresponding author. Tel.: +91 5712703893.

E-mail address: farukh\_arjmand@yahoo.co.in (F. Arjmand).

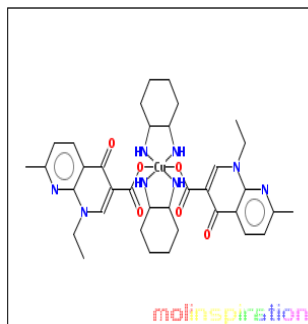
**Figures:**



**(a)**

molinspiration

miSMILES CCn7cc(C(=O)O[Cu]4B(OC(=O)c2cn(CC)c1nc(C)ccc1c2=O)(NC3CCCCC3N4)NC5CCCCC5N6)c(=O)c8ccc(C)nc78



Molinspiration property engine v2013.09

miLogP	2.386
TPSA	170.512
natoms	51.0
MW	750.36
nON	14
nOHNH	4
nviolations	2
nrotb	8
volume	652.332

[Get data as text](#) (for copy / paste).[Get 3D geometry](#) BETA

(b)

**Fig. S1.** Virtual screening of complex **1** showing drug-likeness by (a) Osiris property explorer (b) Molinspiration

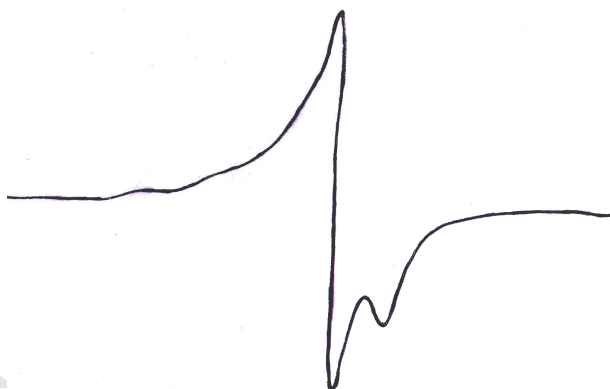


**Fig. S2.** X-band EPR spectrum of complex **1** at LNT.

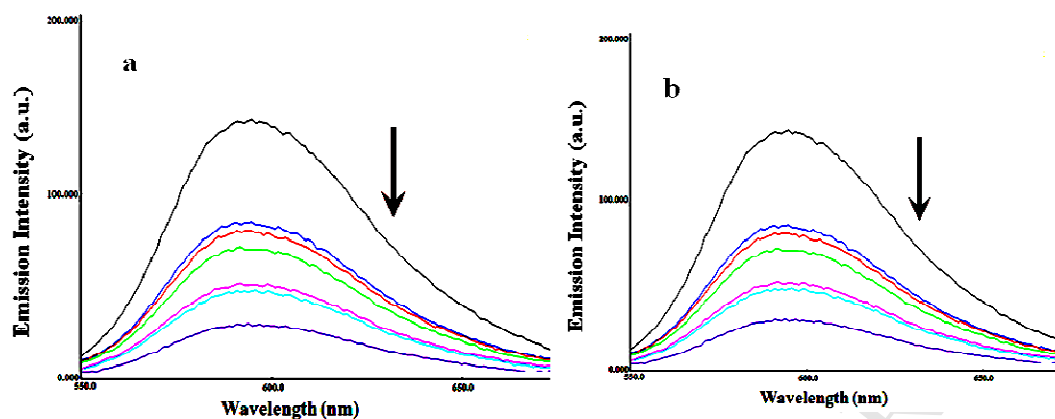


**Fig. S3.** Emission spectra of (a) EB-ct DNA (b) EB-yeast tRNA in the absence and presence of complex **1** at 25 °C in Tris-HCl buffer at pH 7.2. [Complex **1**] = [DNA] = [tRNA] =  $10^{-5}$  M. Arrow shows change in intensity with increasing concentration of ethidium bromide.

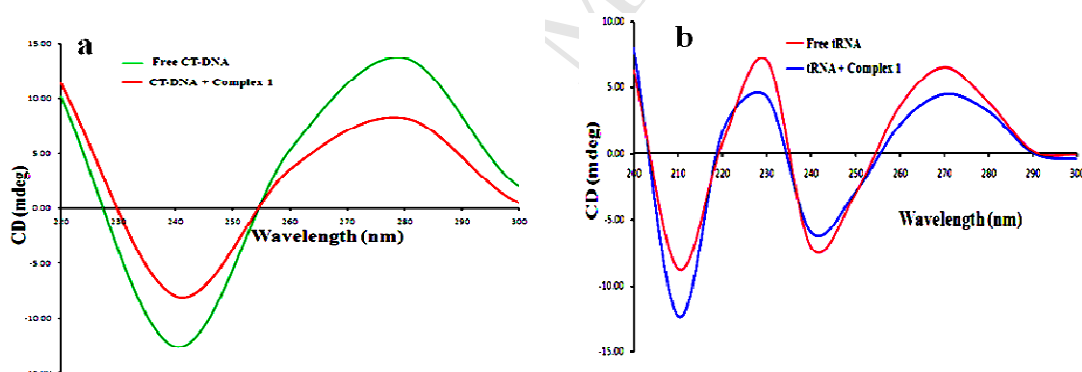


**Fig. S4.** CD spectra of (a) ct-DNA in absence and presence of complex **1** and (b) yeast tRNA in absence and presence of complex **1**. [Complex **1**] = [DNA] = [RNA] =  $10^{-4}$  M.

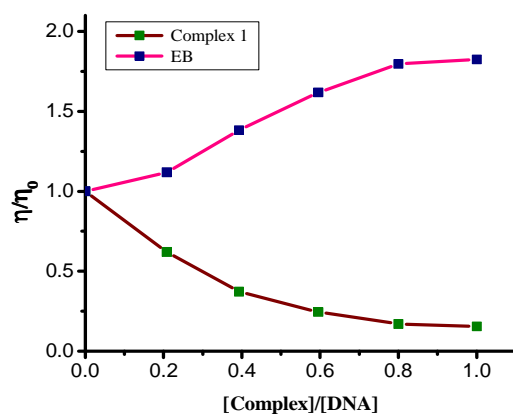


**Fig. S5.** Effect of increasing amount of complex **1** and EB on the relative viscosities ( $\eta/\eta_0$ ) of ct-DNA at 25 °C in Tris-HCl buffer at pH 7.2. The concentration of ct-DNA was 0.10mM, and the molar ratios of complex **1** or EB to DNA were 0.2, 0.4, 0.6, 0.8 and 1.0, respectively.

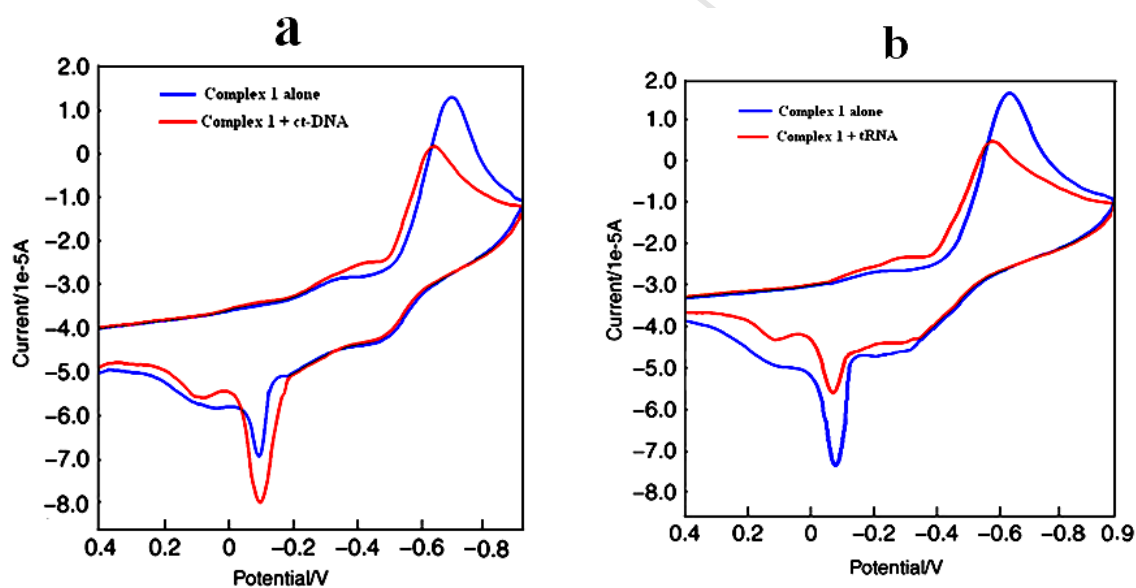


**Fig.S6.** Cyclic voltammogram of complex **1** in MeOH: H<sub>2</sub>O (5:95) at 30 °C at a scan rate of 0.2 V s<sup>-1</sup> (a) in presence and absence of ct-DNA (b) in presence and absence of yeast tRNA.

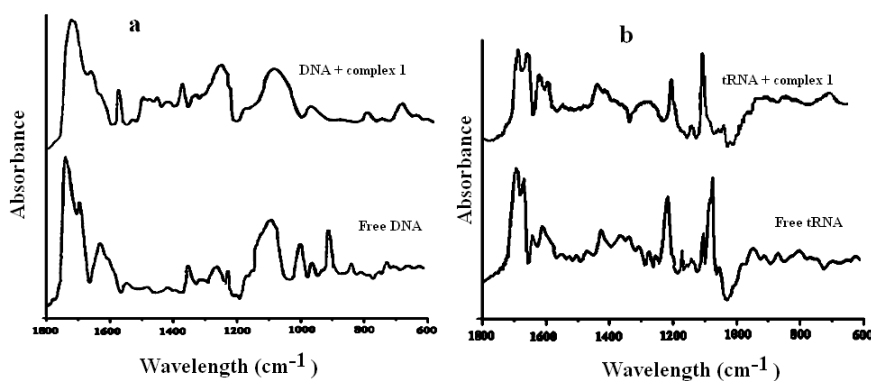


**Fig.S7.** FT-IR spectra and difference spectra [(ct-DNA/tRNA + complex **1**) solution-complex **1** solution] in the region of 1800–800  $\text{cm}^{-1}$  for (a) free ct-DNA and in presence of complex **1** (b) free yeast tRNA and in presence of complex **1**

## Tables

**Table S1:** Selected bond lengths ( $\text{\AA}$ ) and angles ( $^{\circ}$ ) for complex **1**.

Bond lengths	( $\text{\AA}$ )
Cu(1)-N(1)#1	2.0091(19)
Cu(1)-N(2)#1	2.0117(18)
Cu(1)-N(2)	2.0117(18)
N(1)-C(1)	1.473(3)
N(1)-H(1A)	0.9200
N(1)-H(1B)	0.9200
N(2)-C(2)	1.478(3)
N(2)-H(2A)	0.9200
N(2)-H(2B)	0.9200
C(2)-N(2)-Cu(1)	108.26(13)
C(2)-N(2)-H(2A)	110.0
Bond Angles ( $^{\circ}$ )	
N(1)#1-Cu(1)-N(1)	180.000(1)
N(1)#1-Cu(1)-N(2)#1	84.51(7)
N(1)-Cu(1)-N(2)#1	95.49(7)
N(1)#1-Cu(1)-N(2)	95.49(7)
N(1)-Cu(1)-N(2)	84.51(7)
N(2)#1-Cu(1)-N(2)	180.0
C(1)-N(1)-Cu(1)	109.73(14)
Cu(1)-N(2)-H(2A)	110.0
C(2)-N(2)-H(2B)	110.0
Cu(1)-N(2)-H(2B)	110.0
H(2A)-N(2)-H(2B)	108.4
C(7)-N(3)-C(14)	119.53(19)
C(7)-N(3)-C(17)	119.6(2)